Depositional sedimentary environment and hydrothermal controls on organic matter enrichment in the Lower Cambrian Niutitang shale reservoir, South China

Tan, Jingqiang; Wang, Zhangwu; Wang, Wenhui; Hilton, Jason; Guo, Jianhua; Wang, Xikai

DOI:
10.1306/12222018196

Document Version
Peer reviewed version

Depositional environment and hydrothermal controls on organic matter enrichment in the lower Cambrian Niutitang shale, South China

Jingqiang Tan[1,2], Zhanghu Wang [1,2], Wenhui Wang[1,2], Jason Hilton[3], Jianhua Guo[1,2], Xikai Wang[1,2]

1. Key Laboratory of Metallogenic Prediction of Nonferrous Metals and Geological Environment Monitoring, Ministry of Education, School of Geosciences and Info-physics, Central South University, Changsha, 410083, China
2. Hunan Key Laboratory of Nonferrous Resources and Geological Hazards Exploration, Changsha 410083, China
3. School of Geography, Earth and Environmental Science, University of Birmingham, Birmingham, B15 2TT, UK

ACKNOWLEDGMENTS

This work was supported by the National Natural Science Foundation of China (Grants 41872151, 41772001, 41402010), the Fundamental Research Funds for the Central Universities of Central South University (Grant 502221901), and the Innovation-driven Project of Central South University (Grant 502501005). We thank Barry Katz, Robert Merrill, Thomas Algeo and two anonymous reviewers for helpful and constructive comments on earlier versions of the manuscript.

ABSTRACT

The purpose of this research was to examine paleoenvironments, hydrothermal activity, and seawater restriction of the lower Cambrian Niutitang Formation shale gas reservoir in the eastern Xuefeng Uplift and to determine factors affecting organic matter (OM) enrichment. In the studied borehole (X1) in western Hunan Province, the Niutitang Formation can be subdivided into the Niu1, Niu2, and Niu3 members based on geological and geochemical features, including trace element enrichment, lithology and fossil content. Total organic carbon (TOC) values of the Niutitang Formation are variable, averaging 1.5 wt.% in the Niu1 Member, 12.7 wt.% in the Niu2 Member, and 5.1 wt.% in the Niu3 Member. Paleoclimatic changes were responsible for changes in biota, which impacted patterns of OM enrichment. Climate proxies (Chemical Index of Alteration (CIA)), and productivity proxies (Ba_{bio}, Cu/Al, and Ni/Al) consistently indicate higher paleoproductivity in the Niu2 Member. The Niu1 and Niu2 members were possibly affected by hydrothermal events, whereas hydrothermal activity was absent during deposition of the Niu3 Member. Hydrothermal activity may not only provide nutrients and silica but alsoenhance the reducing condition of the water column. In addition, hydrothermal events may have possibly influenced biological survival in the different environments, which in turn increased their reproduction within the early Cambrian ocean and affected OM production. Redox proxies (Mo_{EF} and U_{EF}) imply that the Niu1, Niu2, and Niu3 members were deposited in suboxic, euxinic, and ferruginous environments, respectively. Redox conditions, strongly restricted water environments, and

hydrothermal events were conducive to OM enrichment during the early Cambrian.

INTRODUCTION

During the early Cambrian, a marine transgression event resulted in widespread deposition of organic-rich shale across South China. Although the lower Cambrian shales were subsequently eroded in some parts of the Upper Yangtze Region, their present distribution extends across an area of more than 9.0×10^5 km^2 (~3.5×10^5 mi^2) (Zhang et al., 2017). These organic-rich shale intervals are 50–200 m (164–656 ft) thick in many places, with total organic carbon (TOC) contents commonly above 1.0 wt.% and can reach 30 wt.% (Tan et al., 2013; Yu et al., 2017). Over the past decade, organic-rich shale reservoirs in the Upper Yangtze Region have been widely studied for their promising petroleum potential (Hao et al., 2013; Tan et al., 2014a; Bu et al., 2015; Lyu et al., 2018a; Xiao et al., 2018; L. Li et al., 2019). Of these studies, considerable achievements have been made in our understanding of the Niutitang Formation (and its equivalent horizons, including the Qiongzhusi and Jiumenchong formations) shale gas resources. Wells targeting lower Cambrian shale intervals in Sichuan, Guizhou, and Hubei provinces have already obtained commercial scale shale gas flow. In 2017, the China Geological Survey (CGS) drilled the EYiYe-1 well in Yichang, west Hubei Province, and achieved a production rate of 2.1 MMcf per day (MMcf/d) and an open gas flow rate of 4.4 MMcf/d.

Previous studies on the Niutitang Formation have primarily focused on shale reservoir characteristics and gas potential (Tan et al., 2014b; Tian et al., 2015; T. Lin et al., 2016; J. Yan et al., 2016; Lyu et al., 2018b; Sun et al., 2018). However, the effects of hydrothermal events and depositional environment on organic matter (OM)

enrichment of the Niutitang shale have, by comparison, been overlooked (Liu et al., 2015; Yeasmin et al., 2017; Gao et al., 2018). OM enrichment mechanisms in marine shales are complex and influenced by various factors, including terrigenous detrital supply, paleoclimate, primary productivity, hydrothermal activity, redox conditions, and seawater restriction (Piper et al., 2004; Liu et al., 2015; Wu et al., 2016). Variations in paleoclimate have a marked impact on the abundance of organisms in marine settings and thus influence the supply of OM, while the preservation of OM is controlled by redox conditions, terrigenous dilution, and seawater restriction. The OM supply can be affected by hydrothermal activity, in addition to primary productivity and influences from preservation conditions (Knoll and Carroll, 1999; Reysenbach and Cady, 2001; Little and Vrijenhoek, 2003; Simoneit, 2004; R. Yang et al., 2008; Lane et al., 2010; Fuchida et al., 2014; Y. Li et al., 2015; Han et al., 2017).

In South China, hydrothermal activity mainly occurred during the deposition of the lower part of the Niutitang shale (R. Yang et al., 2008; D. Chen et al., 2009; Y. Li et al., 2015; Liu et al., 2015; Han et al., 2017), whereas the upper part of the Niutitang shale was not obviously affected. Submarine hydrothermal activity with abundant metals and volatile gases (CH_4 and H_2S) may change the redox and chemical conditions of seawater and affect the reproduction of biological communities (Jones and Gislason, 2008; Chambers et al., 2013). The relationship between hydrothermal activity and biological productivity is, nevertheless, not fully understood. Investigations are also relatively rare on the links between seawater restriction and organic-rich shales. The depositional environments during the different time intervals

of the early Cambrian could result in markedly different OM enrichment mechanisms. Previously studied profiles were principally deposited in shallow-deep shelf environments, i.e., Guizhou Province (Y. Li et al., 2015). To examine the correlation between the depositional environments and OM enrichment, freshly cored shale samples that were deposited in deep marine settings were investigated in detail in the current research.

The primary objective of this study was to reconstruct sedimentary environment, hydrothermal activity, and their influences on OM enrichment during shale deposition from the eastern Xuefeng Uplift in the lower Cambrian Niutitang shale. To illustrate the primary factors influencing OM enrichment, a series of analyses including lithofacies, mineralogy, trace and major elements, and TOC were undertaken on shale samples from the recently drilled X1well in Anhua County, Hunan Province, South China (Figure 1).

GEOLOGICAL SETTING

During the late Ediacaran to early Cambrian, the South China Craton consisted of the Yangtze and Cathaysia blocks. From the northwest to the southeast, sedimentary facies comprised marine platform, shallow shelf, deep shelf, slope, and marine basin settings (Goldberg et al., 2007; S. Wang et al., 2015) (Figure 1A). The lower Cambrian sedimentary rocks in the shallow-water areas were primarily composed of dolomite and limestone (e.g., Zhujiaqing and Madiping formations), whereas those sedimentary rocks in deep-water areas principally consisted of siliceous- and

organic-rich shale (e.g., Liuchapo Formation and the lower part of the Niutitang Formation) (Figures 1 and 2). The lower Cambrian interval includes the Cambrian evolutionary radiation of small shelly fossil assemblages (including brachiopods, gastropods and trilobites) and marine plankton (including algae and other microfossils) (R. Yang et al., 2008), providing significant OM inputs into marine depositional settings.

During the late Cambrian Stage 2 (Figure 2), as a result of the breakup of the Rodinia Supercontinent, the Yangtze and Cathaysia blocks commenced rifting. In South China, a major transgression occurred, as well as extensive hydrothermal and volcanic activity (Steiner et al., 2001; D. Chen et al., 2009; Han et al., 2017). Volcanic tuffs and metal ore layers (Ni-Mo, V, and Ba) were widely distributed in the Yu'anshan and Niutitang formations. Black carbonaceous shales were widely developed in the research area as a result of anoxic events in the sedimentary basin, in addition to phosphatic nodules, pyrite, and siliceous shales (Steiner et al., 2007; Wu et al., 2017). Due to paleogeographic differences, the thicknesses and TOC contents of the Niutitang shale vary considerably among its different locations (Figure 2).

The Xuefeng Uplift represents the transitional zone between the Yangtze and Cathaysia tectonic blocks. Sedimentary strata from the Cambrian to the Silurian were extensively developed in the eastern Xuefeng area. The Niutitang shales in the eastern Xuefeng Uplift are characterized by their great thicknesses, high TOC contents, and advanced thermal maturities (T. Lin et al., 2016; J. Chen et al., 2017). Several lower Cambrian sections have been previously studied in detail for volcanic and

biostratigraphic analyses, including the Xiaotan section in Yunnan Province (A. Yang et al., 2003; Steiner et al., 2007; Compston et al., 2008; Och et al., 2013; Jin et al., 2016; C. Yang et al., 2018), the Songtao section in Guizhou Province (A. Yang et al., 2003; Goldberg et al., 2007; D. Chen et al., 2015), the Longbizui section in Hunan Province (J. Wang et al., 2012; C. Yang et al., 2017), and the Ganziping section in Hunan Province (D. Chen et al., 2009), distributed across shallow shelf facies in the west to slope facies in the east (Figure 2).

In 2017, a new test well was drilled in Anhua County, Hunan Province. From the bottom up, the lower Cambrian consisted of the Liuchapo, Niutitang, and Wunitang formations. The present investigation focused on the Niutitang Formation, which has previously been subdivided into three intervals based on the distribution of metal ore layers (Ni-Mo, V, and Ba), carbonaceous shale, tuff, and fossils (Jin et al., 2016). The boundary between intervals I and II is primarily characterized by Ni-Mo layers, carbonaceous shale, and small shelly fossil assemblages (SSF1-4 of Steiner et al. (2007)). The geochronology of the Ni-Mo layer deposited in the transition period between Stages 2 and 3 of the Cambrian is dated to 521±5Ma, based on the Re-Os isochron age (Xu et al., 2011). Shales with high TOC contents are frequently present at the bottom of the Niutitang Formation and close to the metal ore layers. The Niutitang Formation can be subdivided into three members, here named the Niu1, Niu2 and Niu3 members. The lowermost Niu1 Member chiefly consists of dark gray calcareous shales with calcareous patches (Figures 3A and B), with dolomite present at the top of the member (Table 1). The Niu2 Member consists of black siliceous shale,

156 whereas the Niu3 Member principally consists of gray-black shales (Figures 3C and
157 D). However, small shelly fossils are not obvious in the study area. The boundary of
158 the Niu1 and Niu2 members can be characterized by a Ni-Mo layer and lithology. The
159 boundary between Niu2 and Niu3 can be identified according to the relative
160 concentration of trace metals (Mo, V, and U), lithology, and biota (Jin et al., 2016).
161 Trace metal elements of the Niu2 shale are much higher than those of the Niu3 shale
162 by more than one order of magnitude. The trace element values were also consistent
163 with four other sections and wells, including the Xy1 well (J. Li et al., 2018), the
164 Jinsha (Jin et al., 2016), and Dingtai sections (Xu et al., 2012) in the deep shelf facies,
165 and the Yk1 well in slope facies (Y. Li et al., 2015). The three members of the
166 Niutitang Formation can be identified from the GR/API results (Figure 1), with the
167 Niu2 Member having higher values than the Niu1 and Niu3 members. GR/API results
168 have also been applied to the Xy1 and Yk1 wells (Y. Li et al., 2015) and may
169 represent an important method for identifying the members in other well cores.
170 Through geological history, the study area underwent multiple periods of
171 tectonic movement, resulting in thrusting, folding, uplift, and denudation. The
172 (prototype) Nanhua basin was shaped during the Ediacaran, but marine deposition
173 dominated from the early Cambrian to the Triassic. After the mid-Triassic, the basin
174 was uplifted and significantly altered, forming a series of thrust nappes and
175 para-foreland basins (Wan et al., 2018). The Indosinian (257–205 Ma), Yanshanian
176 (199.6–133.9 Ma), and Himalayan (23 Ma-present) orogenies strongly influenced the
177 study area and formed many narrow anticlines and wide synclines. At present, the

outcrops of sedimentary rocks in western Hunan are mainly Paleozoic and Mesozoic in age, and extend in a NE-SW direction. These strata form a compound syncline, with the Cambrian-Silurian rocks in the northwest and southeast, while the Devonian-Middle Triassic rocks are principally located in the center.

MATERIALS AND METHODS

Samples were collected from the X1 well in west Hunan Province (Figures 1B and C). The Liuchapo Formation occurs at the bottom of the well core and consists primarily of a series of gray-black cherts. Pyrite is abundant within the Niutitang shale and occurs as nodules, veins and star spots (Figures 3E and F). The overlying Wunitang Formation consists of dark gray, muddy limestones intercalated with shales.

Samples were taken from the chert and organic-rich shale interval of the core at a spacing of 5–6 m (16–20 ft). A total of 4 Liuchapo chert and 28 Niutitang shale samples were analyzed. Individual samples were ground to less than 100 mesh for analyses of mineralogy and TOC and to below 200 mesh for analyses of trace and major elements.

X-ray diffraction (XRD) measurements were conducted at the Chongqing Mineral Resources Supervision and Test Center using a Bruker D8 Advance diffractometer equipped with a Cu-target tube and a curved graphite monochromator. Measurements were performed at 40 kV and 40 mA. Samples were step-scanned from 3–45° with 0.02° (2θ)/steps.

To determine TOC values, 200 mg of sample was weighed and placed into a

combustion crucible. Excess hydrochloric acid (volume ratio 1:7) was added to remove inorganic carbon. The crucible was then dried in an oven for 1h at 105 ℃ under vacuum conditions. The TOC content was analyzed using a Multi N/C 3100 Analyzer (Germany). The analytical errors were better than ±0.2 %.

For elemental analysis, the sample powder was dried in an oven for 2 h at 105 ℃ under vacuum conditions. To measure the major elements, 500 mg of dried sample was oxidized with 7 g of lithium borate (mixture of 67 % $Li_2B_4O_7$ and 33 % anhydrous $LiBO_2$) for 2 h at 200 ℃, and then the mixture was melted to make a fused glass disk. Measurements were conducted using an Axios MAX pw4400/40 X-ray fluorescence spectrometer. Major elements were represented by oxides (SiO_2, Al_2O_3, FeO, CaO, Fe_2O_3, K_2O, MgO, MnO, Na_2O, P_2O_5 and TiO_2). To determine trace elements, including Th, U, V, Ni, Co, Ba, Sr, Mo, Cu and Cr, 50 mg of dried sample was weighed and treated using boric acid. Trace elements were then determined with quadrupole inductively coupled plasma-mass spectrometry (ICP-MS). The analytical errors were better than ±5 %.

Enrichment factors (EF) were calculated based on the ratio between trace element and aluminum (Al) concentrations of the sample. The same ratio in the Post-Archean Australian Shale (PAAS, Taylor and McLennan, 1985). The following formula was used for this calculation:

$$X_{EF} = (X_{sample}/Al_{sample})/ (X_{PAAS}/Al_{PAAS}) \quad (1)$$

where X_{sample} and Al_{sample} are concentrations of trace element X and Al samples, respectively; X_{PAAS} and Al_{PAAS} are concentrations of trace element X and Al in the PAAS, respectively. X_{EF} >1.0 and X_{EF} <1.0 indicate enrichment and depletion in the X element, respectively.

RESULTS

Mineral Composition

Quartz, feldspar, calcite, dolomite, pyrite and clay are the principal minerals (Table 1). Except for certain Niu1 samples, all samples show >60 % of brittle minerals (e.g., quartz, feldspar, and pyrite), while typically <30 % are ductile minerals (i.e., clay minerals). Quartz dominates the mineral content ($\overline{x}$=61.0 %), whereas the average contents of feldspar and carbonates are much lower at 4.3 %, and 7.5 %, respectively (Figure 4). Two samples from the boundary between the Niu1 and Niu2 members include barite (2.7 %) and glauberite (3.8 % and 29.0 wt.%). The quartz content of Liuchapo chert generally exceeds 94 %.

TOC Content

The TOC content varies from 0.1–20.1 wt.% (Table 2). The TOC generally increases from the Niu1 Member (0.1-4.0 wt.%, mean($\overline{x}$)=1.5 wt.%) to the Niu2 Member (8.1–20.1 wt.%, $\overline{x}$=12.7 wt.%) and then decreases to the Niu3 Member (2.6–8.1 wt.%, $\overline{x}$=5.1 wt.%) (Figure 5). The TOC contents of the Liuchapo cherts are lower than 0.4 wt.%.

244

245 **Major Element Composition**

246 The major element compositions show considerable variations among the three
247 members (Table 2). Except for a dolomite sample, the elements of the analyzed shale
248 samples are dominated by SiO_2 (30–74 %). The SiO_2 concentrations are commonly
249 higher in the Niu2 and Niu3 samples than in the Niu1 samples. The Al_2O_3
250 concentrations are variable for the Niu1 samples, ranging from 2–17 %. Most of the
251 Niu2 samples show Al_2O_3 contents below 6 %, while all Niu3 samples show Al_2O_3
252 contents higher than 6%. The Fe_2O_3 concentrations are below 5 % for all analyzed
253 samples, with the Niu3 samples showing higher values than those of the Niu1 and
254 Niu2 samples. Compared to the Niu2 and Niu3 shales, the Niu1 shale samples contain
255 relatively high MgO and CaO concentrations that can reach >10 %. In addition, the
256 K_2O concentration of in the Niu2 samples is relatively lower than that in the Niu1 and
257 Niu3 shales. Commonly, the FeO, TiO_2, Na_2O, P_2O_5, and MnO contents are below
258 1 %.

259

260 **Trace Element Composition**

261 Trace element values are given in Tables 3 and 4. The Cu, Ni, and Ba contents are
262 typically high in the Niu2 samples, moderate in the Niu3 samples, and low in the
263 Niu1 samples. Compared to the Liuchapo chert samples, the Niutitang samples are
264 rich in Mo, U, and V. The enrichment factors of these three redox elements vary
265 significantly (Table 4). The Niu1 samples are weakly enriched with Mo (Mo_{EF}: 3–

244), V (V_{EF}: 1–17), and U (U_{EF}: 6–31). The enrichment of these three elements is stronger in the Niu2 samples (Mo_{EF}: 168–1265, V_{EF}:6–129, and U_{EF}:31–657) and moderate in the Niu3 samples (Mo_{EF}: 42–161, V_{EF}:1–4, and U_{EF}:5–31).

DISCUSSION

Paleoclimate

Paleoclimate can greatly influence marine productivity, redox conditions, and the supply of terrestrial materials. From an analysis of paleomagnetism, South China was inferred to be located in a subtropical-tropical zone near the equator during the early Cambrian (Mckerrow et al., 1992; Yeasmin et al., 2017). Quantitative information on the paleoclimatic conditions can be interpreted from geochemical proxies because trace elements in sedimentary rocks are sensitive paleoclimate indicators in several cases (Galloway et al., 2013; Vosoughi Moradi et al., 2016; Yeasmin et al., 2017).

The Chemical Index of Alteration (CIA) is used to identify climate conditions in deep time (Nesbitt and Young, 1982). CIA values from 50–65 indicate cold climates with weak chemical weathering, from 65–85 indicate warm and humid climates with moderate weathering, and from 85–100 represent hot and humid climates with strong weathering (Nesbitt and Young, 1982; Cole et al., 2009). Furthermore, CIA is also related to the parent rock type; when carbonate parent rocks dominate, the ratio is relatively low (Zhai et al., 2018). CIA is calculated using the molar oxides according to the following formula:

$$CIA = [Al_2O_3/(Al_2O_3+CaO^*+Na_2O+K_2O)] \times 100 \quad (2)$$

where CaO^* was corrected by using P_2O_5 data ($CaO^* = CaO-10/3 \times P_2O_5$). If the content of CaO was less than that of Na_2O, the CaO value was used as CaO^*. In contrast, CaO^* was assumed to be equivalent to Na_2O (McLennan, 1993; Fedo et al., 1995; Zhai et al., 2018).

In this research, the lithology of the Niu1 Member is principally calcareous shale (Table 2). The calculated CIA values of the Niu1 samples are relatively low (mean($\bar{x}$)=71) but should have been affected by the high carbonate contents (Figure 5). A detailed explanation of the entire Niu1 interval is thus complex based on CIA values alone. Nevertheless, glauberite occurs in the upper part of the Niu1 Member and the lower part of Niu2 Member. This suggests arid and hot climates (L. Wang et al., 2013). The average CIA value of all Niu2 shales is 75, and that of the Niu3 shales is 75. Because shale samples from these two intervals contain few carbonate minerals, CIA values indicate that the climate was warm and humid. Overall, the CIA results indicate that climate fluctuations occurred during the early Cambrian (Figure 5). Warm climates in the Niu2 and Niu3 members are more conducive to greater biomass than conditions occurring during the Niu1 Member.

Redox Conditions

Anoxic conditions are more conducive to OM preservation because of weak degradation (Tribovillard et al., 2012; Ocubalidet et al., 2018). The Niu2 Member

shale samples are rich in pyrite (Figures 3E and F), reflecting that the water column is dominated by reducing conditions. The trace elements Mo, U and V are sensitive to redox conditions in sedimentary environments and hardly migrate during diagenesis; they are excellent proxies for reconstructing redox conditions (Algeo and Maynard, 2008; Algeo and Tribovillard, 2009; Algeo and Rowe, 2012; Wu et al., 2016). The precipitation of U occurred earlier than that of Mo in the suboxic environment. In this study, we rely on Mo geochemistry (Scott and Lyons, 2012) and trace metal enrichment (Mo_{EF} and U_{EF}) (Tribovillard et al., 2006; Algeo and Tribovillard, 2009) as paleoredox proxies.

Previous studies on modern oceans have shown that Mo contents less than 25 ppm, between 25–100 ppm, and more than 100 ppm indicate non-euxinic, intermittent, and strongly euxinic environments, respectively (Scott and Lyons, 2012). In this research, all Niu1 samples show Mo contents below 25 ppm ($\overline{x}$ = 8.3 ppm), indicating the predominance of non-euxinic environments (Figure 5). The Mo contents of the Niu2 samples are variable, ranging from 18.0–209.0 ppm ($\overline{x}$ = 83.4 ppm). Although there are two samples below 25 ppm, most Niu2 samples have Mo contents exceeding 50 ppm or even 100 ppm, suggesting intermittent euxinic/euxinic environments. The Mo contents of most Niu3 samples are above 25 ppm but below 100 ppm (ranging from 24.3–76.2 ppm, $\overline{x}$ = 40.3 ppm), indicating the predominance of intermittent euxinic environments. In addition, shale samples fall into different zones on the covariation plot of Mo_{EF} - U_{EF}, indicating different sedimentary environments (Figure 7). Niu1 shales were deposited under primarily suboxic conditions, as shown by the

weak enrichment of Mo and U (i.e., low Mo_{EF} and U_{EF}). In contrast, the $Mo_{EF} - U_{EF}$ of all Niu2 samples are high, and those of the Niu3 samples are moderate, indicating that the shales were deposited under primarily oxygen-depleted conditions, i.e., euxinic and ferruginous (e.g., anoxic) environments (Algeo and Li., 2020). These conclusions are consistent with the Mo geochemistry observed.

The redox conditions in the early Cambrian were also related to sea level changes. During Niu1 shale deposition, there was a short-term marine regression with seawater shallowing and becoming oxygen-rich (Figure 5). Subsequently, as the sea level increased, the oxygen content decreased in the seawater; thus, reducing conditions during Niu2 and Niu3 deposition increased. The ferruginous-euxinic threshold of this study is 10 wt.% (e.g., TOC). Pi et al. (2013) reported a threshold value of 5 wt.% because of differences in terrigenous dilution and marine paleoproductivity. TOC content vs Mo/Al ($r = +0.44$, $p(a) < 0.05$, $n = 28$) (Figure 8A) and TOC content vs V/Al ($r = +0.73$, $p(a) < 0.01$, $n = 28$) (Figure 8B) demonstrate that redox conditions are conducive to OM enrichment in the Niutitang shale. Consequently, all selected parameters suggest that the reduction strength in the early Cambrian was in the order of Niu2>Niu3>Niu1.

Terrigenous Debris

All analyzed shale samples contain a high proportion of quartz, with an average content of 65 % (Table 1). Siliceous minerals can be derived from terrestrial,

353 hydrothermal, or biogenic origins (Pi et al., 2013; X. Yang et al., 2018). Al and Ti are
354 mainly related to terrigenous detritus (Wedepohl, 1971). In the Niutitang shale
355 samples, the correlation between Al_2O_3 and SiO_2 is very weak (Figure 9A), indicating
356 that the silica may not be largely derived from continental sources. In addition to
357 terrigenous origins, a large amount of silica in the shales must therefore originate
358 from other sources. The Al_2O_3 contents in the Niutitang shales are highly variable
359 (Table 1), with the Niu1 Member ($\bar{x}$=6.8 %) > Niu2 Member ($\bar{x}$=3.8 %) < the Niu3
360 Member ($\bar{x}$=9.9 %). This suggests that the distance of Niu2 shales from the clastic
361 source was greater than that distance of either the Niu1 or Niu3 shales. In addition,
362 the TOC contents also show negative correlations with the TiO_2 contents, indicating
363 the terrigenous dilution of OM (Figure 9B).
364
365 **Hydrothermal Sedimentation Processes**
366 The Al/(Al+Mn+Fe) ratio is used to determine siliceous origins (Adachi et al., 1986;
367 Yamamoto, 1987), with a pure hydrothermal activity ratio of 0.01 and a pure biogenic
368 origin having a ratio of more than 0.60 (Yamamoto, 1987; Harris et al., 2011). In
369 addition, biogenic shales are characterized by high SiO_2 and P_2O_5 values and low
370 Al_2O_3, TiO_2, and MgO values, whereas the enrichment of Fe and Mn is mainly related
371 to hydrothermal activity (X. Wang et al., 2016; Liao et al., 2018). Similarly, the
372 (Fe+Mn)/Ti ratio is an index for determining conditions of hydrothermal deposition.
373 Typical hydrothermal deposits are characterized by Al/(Al+Mn+Fe) <0.4 and
374 (Fe+Mn)/Ti >15 (Adachi et al., 1986). Niutitang shale samples fall in the different

zones on an Al-Fe-Mn ternary diagram (Figure 10), indicating that the silica comes from different origins. Cherts from the Liuchapo Formation exhibit low Al/(Al+Mn+Fe) ratio values (0.1–0.3), and high (Fe+Mn)/Ti ratio values (18.1–37.7), suggesting intense hydrothermal activity (Figure 6). Rare earth element geochemistry of the Liuchapo cherts also suggests that intense hydrothermal activity occurred in the deep water area (Guo et al., 2016). Siliceous genesis of the Niu1 and Niu2 members mainly relates to intense hydrothermal activity (Al/(Al+Mn+Fe) = 0.4–0.8, (Fe+Mn)/Ti = 5.6–17.9), whereas that of the Niu3 Member relates more to non-hydrothermal origins (Al/(Al+Mn+Fe) > 0.60, (Fe+Mn)/Ti < 15). Z. Wang et al., (2020) also found that hyalophane was developed at different depths in the Niu1 and Niu2 shales. The hyalophane with another minerals (e.g., spehalerite and monazite) can be an important proxy for hydrothermal activity. These results are in accordance with the discovery of volcanic material (Figure 2), hydrothermal vent communities and hydrothermal minerals at the bottom of the Niutitang Formation (R. Yang et al., 2008; Han et al., 2017). The comparison of rare earth elements (Eu anomalies) in several sections from South China also confirms that hydrothermal activity occurred during the early Cambrian (Guo et al., 2016; Gao et al., 2018).

In general, the non-detrital fraction of a given element can be estimated by subtracting the detrital fraction from the total amount of the element. Regarding Si, we assume that all excess Si in the non-detrital fraction and is entirely derived from either hydrothermal or biological origins. The calculations for Si_{excess} and $SiO_{2excess}$ are:

$$Si_{excess} = Si_{sample} - (Si/Al)_{background} \times Al_{sample} \quad (3)$$

$$SiO_{2excess} = SiO_{2\ sample} - [(Si/Al)_{background} \times Al_{sample}] \times 60.1/28.1 \quad (4)$$

where Si_{excess} represents the non-detrital silicon content, Si_{sample} represents the silicon concentration in the sample, Al_{sample} represents the Al concentration in the sample and the (Si/Al) background value is 3.11 (Wedepohl, 1971).

According to Figure 5, excess silica amounts increase from the top of the Niu1 to Niu2 members and then decrease in the Niu3 Member. The excess silica contents of the Niu1 Member vary from 0–49.0 % ($\overline{x}$=23.8 %). The contents of the Niu2 samples are commonly high, between 41.4 % and 77.6 % ($\overline{x}$=57.5 %), while those of the Niu3 samples are moderate, varying from 27.6–50.3 % ($\overline{x}$=35.3 %). This implies that a large proportion of silica should be of either a hydrothermal or biogenic origin, with a certain amount of silica originating from terrigenous detritus. In addition, the origin of chert and the source of silica during the Ediacaran-Cambrian transition are still widely disputed. It has been argued that excess silica in shales may be related to hydrothermal activity and also continental weathering (D. Chen et al., 2009; D. Lin et al., 2015; Liu et al., 2015). In this research, although the CIA values suggest moderate weathering during deposition of the Niu2 and Niu3 members, the CIA values do not correlate with the excess silica contents observed, even for samples deposited under the shallowest water conditions (e.g. in the Niu1 Member) (Figure 11A). This indicates insignificant influences of continental weathering on silica enrichment in the

analyzed samples. In contrast, the excess silica content positively correlates with the ratios of Al/(Fe+Al+Mn) (Figure 11B), implying that the silica contents were affected by hydrothermal events. The correlations between excess silica and TOC contents are significant for the Niu3 samples (Figure 11C), but are unclear for the Niu1 and Niu2 samples (Figure 11D). Organisms most likely thrived during the deposition of Niu3 and provided biogenic silica. However, the silica sources of the Niu1 and Niu2 members should be dominated by hydrothermal sources. Liu et al. (2015) analyzed the interbedded layers of chert and shale from the Yangtiao section in Guizhou Province and they concluded that chert and shale intervals were deposited during intense and weak hydrothermal activity, respectively. Strong hydrothermal events could release more silica into the ancient ocean than weaker events, thus forming silica-rich rocks (e.g., chert). Nevertheless, in the early Cambrian hydrothermal events may not only carry silica but also abundant redox-sensitive metal elements into the water column. In the current study, certain redox-sensitive trace elements (Mo, U, and V) from the X1 well and a typical hydrothermal plume from the Mid-Atlantic Ridge were selected to illustrate whether hydrothermal activity affected the redox conditions (German et al., 1991a). Through observations of the Niu3 deposition processes, no obvious hydrothermal activity occurred. Thus, correlations among these three elements of the Niu3 shales are still evident (Figures 12A and B). Correlations among these three elements from the Niu1 and Niu2 shales are all much weaker than those correlations among the three elements of the Niu3 shales (Figures 12C and D), which is consistent with correlations observed in typical hydrothermal samples (Figure 12E).

However, the correlations of the Mo and V elements from the hydrothermal plume are better than those of the X1 well samples (Figure 12F). Previous studies show that V and U concentrations both exhibit pronounced linear correlations with hydrothermal intensity based on samples from the Mid-Atlantic Ridge (German et al., 1991b). Hydrothermal fluid may be conducive to the enrichment of these two elements. In our work, V_{EF} and U_{EF} are relatively high in samples deposited in shallow water conditions (e.g., Niu1 Member) but low in deep water samples (e.g., Niu3 Member). This phenomenon suggests that hydrothermal activity not only provided redox trace elements but also enhanced marine reducing conditions.

Marine Productivity

Paleoproductivity, referring to the amount of OM produced in a certain period of geological history (Taylor, 1964; Gupta and Kawahata, 2006; Tribovillard et al., 2006; Zhao et al., 2017), is typically evaluated using TOC as a proxy. However, TOC is commonly affected by diagenesis, redox reactions, biological action, and the dilution of macerals, which may lead to either over- or underestimates of primary productivity (Gupta and Kawahata, 2006; Tribovillard et al., 2006). Since Ba is an inert element and has a long residence time in oceans, it is commonly used as an auxiliary indicator of paleoproductivity (Taylor, 1964; Böttcher et al., 2003; Schoepfer et al., 2015). In most modern aquatic sediments, Ba mainly exists in the form of $BaSO_4$. There is a significant correlation between Ba content of sediments and biological productivity in

462 the overlying water column. To eliminate the influence of Ba from terrestrial debris,
463 the content of biogenic Ba (Ba_{bio}) is obtained by subtracting the terrestrial fraction
464 from the total Ba. Ba_{bio} is calculated by the formula:
465
466 $$Ba_{bio} = Ba_{sample} - Ba_{detrital} = Ba_{sample} - Al_{sample} \times (Ba/Al_{alu}) \quad (5)$$
467
468 where Ba_{sample} is the Ba concentration in the sample, Al_{sample} is the Al concentration in
469 the sample, and Ba/Al_{alu} is the ratio of Ba and Al in PAAS. The Ba/Al_{alu} ratio is the
470 Ba/Al ratio of the aluminosilicate component ranging from 0.005–0.01 in crustal
471 rocks (Taylor, 1964). A value of 0.0075 is widely used to calculate the contents of
472 Ba_{bio} (Dymond et al., 1992; Zhao et al., 2016). In general, the Niutitang shales exhibit
473 moderate to high degrees of calculated Ba_{bio} contents (38 to 8264 ppm; averaging
474 1382 ppm), compared to those values documented from the modern equatorial Pacific
475 (~1000–5000 ppm) (Murray and Leinen, 1993). The Ba_{bio} contents are variable in the
476 three members, showing mean values of Niu1 ($\overline{x}$=1199 ppm) < Niu2 ($\overline{x}$=1642 ppm) >
477 Niu3 ($\overline{x}$=932 ppm). The Ba and Ba_{bio} contents slowly vary vertically throughout the
478 shale interval, with Niu2 shale samples being slightly more enriched than Niu1 and
479 Niu3 shale samples. The correlation between Ba_{bio} and TOC contents is unclear
480 (Figure 6). This may be caused by the loss in Ba as a consequence of the elevated rate
481 of bacterial sulfate reduction (Schoepfer et al., 2015). During the deposition of Niu3,
482 Ba_{bio} contents were less than 1000 ppm, since $BaSO_4$ was easily reduced under anoxic
483 conditions. Thus, the Ba_{bio} contents of the Niu1 samples that accumulated under

suboxic conditions can be reliably used to evaluate paleoproductivity. Paleoproductivity was relatively high in the Niu1 and Niu2 intervals, and it was moderate in the Niu3 interval.

In addition to biogenic Ba, Ni and Cu can also reflect initial productivity (Calvert and Pedersen, 1993; Algeo and Maynard, 2004; Tribovillard et al., 2006). In modern oceanic sediments, Cu and Ni show positive linear correlations with TOC. As nutrient elements, they either combine with OM or form organic complexes (Froelich et al., 1979; Emerson et al., 1985). High Cu and Ni contents therefore relate to high OM inputs, reflecting higher paleoproductivity (Emerson et al., 1985; Piper and Perkins, 2004; Zhao et al., 2016). To exclude the influence of terrigenous clastic dilution, Cu/Al and Ni/Al ratios were used to characterize paleoproductivity. The Cu/Al and Ni/Al ratios vary to a certain degree in the three members, showing mean values of Niu1 (Cu/Al =8.8 and Ni/Al =8.3) < Niu2 (Cu/Al =77.3 and Ni/Al=73.5) > Niu3 (Cu/Al =10.1 and Ni/Al =16.6) (Figure 6). Paleoproductivity in the Niu2 Member is higher than that in either the Niu1 or Niu3 members, which is consistent with interpretations observed from the biogenic Ba. The TOC contents of the Niu3 shales are generally lower than 10 wt.% (Table 2), with an average of 5.1 wt.%, and close to that of the Longmaxi Formation in the Sichuan Basin (Yan et al., 2012; Feng et al., 2018). Previous studies have shown that silica genesis in the Longmaxi Formation shale is dominated by biological origins, rather than hydrothermal sources (Liu et al., 2017; Luo et al., 2017; Zhao et al., 2017). After demonstrating the existence of hydrothermal events, there is still a need to analyze the effect of hydrothermal activity

on organismal abundance. Hydrothermal activity may not only provide nutrients, but may also affect organismal survival (Z. Wang et al., 2020). The depositional environments of the lower part of the Niutitang Formation were dominated by an intermittent sulfur-containing water column (C. Li et al., 2010; Jin et al., 2016). Chen et al. (2009) analyzed samples from the Ganziping section in Hunan Province (Figure 2) and reported that hydrothermal venting released large amounts of silica-rich hydrothermal fluids with greenhouse gases (methane) and volcanic-derived H_2S into the ocean and/or atmosphere during the early Cambrian. Gao et al. (2018) also documented that hydrothermal venting probably promoted a sulfidic ocean chemistry, which then gradually evolved into a persistent anoxic ocean. The nutrients provided by hydrothermal activity were conducive to the reproduction of phytoplankton (e.g., algae) and thus enhanced the supply of OM (Uematsu et al., 2004; Duggen et al., 2010). Toxic elements (e.g., Hg, Pb, and Cr) and volatile gases (e.g., HCl and SO_2) carried by hydrothermal events could also have inhibited the growth of zooplankton (Jones and Gislason, 2008; Chambers et al., 2013). The decomposition of OM during the deposition process could consume a large amount of oxygen in the water column, and significantly affect living organisms. The ecological imbalance probably strengthened the reducing potential of the water column and in turn was beneficial to the preservation of OM. By analyzing the evolutionary events of early Cambrian organisms, the first stage biota comprises small shelly fossils that became extinct before 521 Ma, while the Chengjiang fauna represents the second stage biota that began to expand at 518.03 ± 0.69 Ma (D. Wang et al., 2018; C. Yang et al., 2018). The

large-scale pervasive oxygenation of the ocean was not the primary control on animal diversity (Jin et al., 2016; Xiang et al., 2017). Hydrothermal activity may inhibit zooplankton reproduction and accelerate phytoplankton reproduction (Z. Wang et al., 2020), as well as increase OM contents in sedimentary rocks. Under reducing conditions, greater OM content in sediment can be preserved. In this research, the TOC content of the Niu2 shale is generally in excess of 10 wt.% and in certain cases up to 20 wt.% (Table 2). Hydrothermal activity may be one of the main reasons for OM enrichment in the Niutitang Formation.

Seawater Restriction

Mo can be used to determine the degree of water restriction in ancient sediments. Mo exists in a stable state with a high valence (+6) in oxygen-enriched water and is difficult to deposit in sediments. However, Mo(VI) can convert from molybdates to thiomolybdates, and be transferred to anoxic sediments (Taylor and McLennan, 1985; Algeo and Tribovillard, 2009). The average Mo content in the upper crust is as low as 3.7 ppm (Zheng et al., 2000; Rowe et al., 2008; Morford et al., 2009; Tribovillard et al., 2012). Furthermore, Mo has a long residence time in water (approximately 780 kyr). This unique feature of Mo is often used to assess the restriction of modern and ancient seawater (Tribovillard et al., 2012; Zhao et al., 2016; Liu et al., 2017). The relationship between Mo and TOC can reveal the degree of anoxic water restriction but not oxic/suboxic conditions. In this research, the Niu1 Member is shown to be

549 dominated by suboxic sedimentary conditions (Figure 13). An oxygen-containing
550 water column was not conducive to the precipitation of Mo, so the Mo contents are
551 commonly low. In addition, the seawater was shallow, and poorly connected to the
552 surrounding ocean such that the environment should be strongly restricted. The
553 Mo/TOC ratio of the bottom part of the Niu2 Member varies from 1.2–5.8, indicating
554 that the water column was strongly restricted close to the values from recent Black
555 Sea sediments (Mo/TOC = 4.5) (Algeo and Lyons, 2006; Tribovillard et al., 2012).
556 However, the Mo/TOC ratio of the upper part of the Niu2 shale is closer to present
557 day values of the Cariaco Basin (Mo/TOC = 25) (Algeo et al., 2007; Tribovillard et al.,
558 2012), indicating a weakly to moderately restricted water environment. With sea level
559 falling, seawater became more restricted in the Niu3 Member, with the Mo/ TOC
560 value of this member becoming close to that of the present day Framvaren Fjord value
561 (Mo/TOC = 9).

562 Although the eastern Xuefeng Uplift experienced euxinic environments during
563 deposition of the Niu2 Member, the shale was also affected by hydrothermal activity.
564 However, the TOC content changes markedly in the vertical direction within the Niu2
565 shale, ranging from 8.1–20.1 wt.% (Table 1). The restricted marine environment may
566 play an important role in the enrichment of OM in shales. The water column was
567 strongly restricted in the lower part of the Niu2 Member, with the seawater isolated to
568 a large degree from the surrounding ocean. This provided a low water exchange rate
569 and allowed the water to carry less oxygen, which was conducive to preserving OM in
570 low oxygenated conditions. As the sea level rose, the water column changed to a

moderately/weakly restricted environment in the upper part of the Niu2 Member. The water exchange rate was faster and the water carried more oxygen, resulting in more OM being degraded under oxygenated conditions. Thus, seawater restriction was also an important factor affecting OM enrichment.

OM Accumulation Mechanism in the Niutitang Formation

The TOC content of the Niutitang shale is variable (Table 2) for which the mechanisms of OM accumulation in the three members are significantly different (Figure 14). In the Niu1 interval, the climate was hot, and marine productivity was comparatively moderate. Weak hydrothermal activity was present. Nutrients and volatile gas entered the water column (Figure 14A), and they slightly advanced the initial productivity and the reducing potential of the seawater. The weak hydrothermal activity had less relative effect on the redox and chemical conditions of the water column. The redox conditions were dominated by suboxic environments. This interpretation is consistent with the lithology analysis (e.g., calcareous shale). OM was easily decomposed and consumed in oxygen-containing seawater and thus was not conducive to preservation. The TOC contents of the Niu1 shale are below 4 wt.%. Thus, redox condition was the main factor controlling OM accumulation during the Niu1 interval.

During the Niu2 interval, the climate was humid and warm, with marine productivity at its highest (Figure 14B). The redox conditions of seawater were dominated by an euxinic environment. Strong hydrothermal activity occurred.

Abundant nutrients and volatile gas entered the water column, and they strongly increased the initial productivity and greatly enhanced the reducing potential of the seawater. The nutrients from hydrothermal activity were conducive to algae thriving, but the euxinic seawater inhibited the survival of zooplankton (e.g., radiolaria). In addition, algal reproduction led to a significant increase in the OM that was deposited and buried in the marine basin. The Niu2 interval can be divided into two parts due to seawater restriction. In the lower part of the Niu2 interval, which is associated with the sea level slowly rising, the water column was gradually transformed into euxinic conditions. Seawater was also strongly restricted, and had poor connectivity with surrounding oceans. The strongly restricted environment could have resulted in a slow exchange rate of oxygen and an enhanced reducing potential, which is similar to the current state of the Black Sea. It also reduced the consumption of OM by limiting oxygen. The TOC contents of the lower Niu2 shales are generally above 13 wt.% and can be up to 20 wt.%. In the upper part of the Niu2 interval, which is associated with the sea level rising, the water column transformed into a weakly restricted environment. The seawater had good connectivity with the surrounding oceans. A rapid exchange of oxygen could have consumed a significant amount of OM. The TOC contents of the upper Niu2 shales are generally greater than 10 wt.%. Overall, the restricted marine environments, redox conditions, and hydrothermal activity enhanced OM enrichment during the deposition of Niu2 shales.

During the Niu3 interval, the climate was similar to that of the Niu2 interval (Figure 14C). The study area changed into a ferruginous environment due to sea level

615 decline. The water column was also moderately restricted, similar to that of the upper
616 Niu2 interval. In addition, hydrothermal activity was not obvious, and led to the
617 restoration of ecological balance. Zooplankton reproduction was not limited. More
618 algae were consumed and thus abated the supply of OM. The reducing potential of the
619 water column had not been strengthened by the other causes introduced. The TOC
620 contents of the Niu3 shales are generally less than 10 wt.%. Redox conditions and
621 moderately restricted environments both played an important role in the preservation
622 of OM.
623

624 **CONCLUSIONS**

625 Based on the analysis of lithofacies, mineralogy, and a series of proxies from major
626 and trace elements in the lower Cambrian Niutitang shale samples from the eastern
627 Xuefeng Uplift, we show that the Niutitang Formation includes three distinct
628 sedimentary periods corresponding to the Niu1, Niu2, and Niu3 members. Redox
629 proxies (Mo geochemistry, Mo_{EF}, and U_{EF}) indicate that the Niu1, Niu2 and Niu3
630 members were deposited in suboxic, euxinic, and ferruginous environments,
631 respectively. Climatic conditions and paleoproductivity proxies (Ba_{bio}, Cu/Al, and
632 Ni/Al) suggested an overall paleoproductivity trend of Niu1 < Niu2 > Niu3.
633 Submarine hydrothermal activity probably appeared in the Niu1 interval, strengthened
634 in the Niu2 interval, and was insignificant in the Niu3 interval. Nutrients provided by
635 hydrothermal activity were conducive to phytoplankton (e.g., algae) thriving and thus
636 increased the OM supply. However, volatile gases (e.g., HCl and SO_2) and euxinic

conditions may inhibit the survival of zooplankton. An ecological imbalance strengthened the reducing potential of the water column that led to a large increase in the amount of OM deposited and buried in marine basins. In addition, due to the variation in sea level, the strongly restricted environment in the early Niu2 interval was more beneficial to the preservation of OM than that occurring in the upper Niu2 and Niu3 intervals. Hydrothermal activity may play a dual role in the supply and preservation of OM, which is the key factor of OM enrichment in the lower Cambrian Niutitang shale.

REFERENCES CITED

Adachi, M., K. Yamamoto, and R. Sugisaki, 1986, Hydrothermal chert and associated siliceous rocks from the northern Pacific their geological significance as indication of ocean ridge activity: Sedimentary Geology, v. 47, no. 1, p. 125–148, doi:10.1016/0037-0738(86)90075-8.

Algeo, T. J., and J. B. Maynard, 2004, Trace–element behavior and redox facies in core shales of Upper Pennsylvanian Kansas-type cyclothems: Chemical Geology, v. 206, no. 3, p. 289–318, doi:10.1016/j.chemgeo.2003.12.009.

Algeo, T. J., and T. W. Lyons, 2006, Mo–total organic carbon covariation in modern anoxic marine environments: Implications for analysis of paleoredox and paleohydrographic conditions: Paleoceanography, v. 21, no. 1, p. 1–23, doi:10.1029/2004PA001112.

Algeo, T. J., T. W. Lyons, R. C. Blakey, and D. J. Over, 2007, Hydrographic conditions of the Devono–Carboniferous North American Seaway inferred from sedimentary Mo–TOC relationships: Palaeogeography, Palaeoclimatology, Palaeoecology, v. 256, no. 3, p. 204–230, doi:10.1016/j.palaeo.2007.02.035.

Algeo, T. J., and J. B. Maynard, 2008, Trace–metal covariation as a guide to water–mass conditions in ancient anoxic marine environments: Geosphere, v. 4, no. 5, p. 872–887, doi:10.1130/GES00174.1.

Algeo, T. J., and N. Tribovillard, 2009, Environmental analysis of paleoceanographic systems based on molybdenum–uranium covariation: Chemical Geology, v. 268, no. 3/4, p. 211–225, doi:10.1016/j.chemgeo.2009.09.001.

Algeo, T. J., and H. Rowe, 2012, Paleoceanographic applications of trace–metal concentration data: Chemical Geology, v. 324, p. 6–18,

doi:10.1016/j.chemgeo.2011.09.002.
Algeo, T. J., and C. Li, 2020, Redox classification and calibration of redox thresholds in sedimentary systems: Geochimica et Cosmochimica Acta, in press, doi: 10.1016/j.gca.2020.01.055.
Böttcher, M. E., J. Rinna, B. Warning, R. Wehausen, M. W. Howell, B. Schnetger, R. Stein, H. J. Brumsack, and J. Rullkötter, 2003, Geochemistry of sediments from the connection between the western and the eastern Mediterranean Sea (Strait of Sicily, ODP Site 963): Palaeogeography, Palaeoclimatology, Palaeoecology, v. 190, p. 165–194, doi:10.1016/S0031-0182(02)00604-1.
Bu, H., Y. Ju, J. Tan, G. Wang, and X. Li, 2015, Fractal characteristics of pores in non–marine shales from the Huainan coalfield, eastern China: Journal of Natural Gas Science and Engineering, v. 24, p. 166–177, doi:10.1016/j.jngse.2015.03.021.
Calvert, S. E., and T. F. Pedersen, 1993, Geochemistry of Recent oxic and anoxic marine sediments: Implications for the geological record: Marine Geology, v. 113, no. 1, p. 67–88, doi:10.1016/0025-3227(93)90150-T.
Chambers, R., A. Candelmo, E. Habeck, M. Poach, D. Wieczorek, K. Cooper, C. Greenfield, and B. Phelan, 2013, Ocean acidification effects in the early life-stages of summer flounder, Paralichthys dentatus: Biogeosciences Discussions, v. 10, no. 8, doi:10.5194/bgd-10-13897-2013.
Chen, D., J. Wang, H. Qing, D. Yan, and L. I. Renwei, 2009, Hydrothermal venting activities in the Early Cambrian, South China: Petrological, geochronological and stable isotopic constraints: Chemical Geology, v. 258, no. 3, p. 168–181, doi:10.1016/j.chemgeo.2008.10.016.
Chen, D., X. Zhou, Y. Fu, J. Wang, and D. Yan, 2015, New U–Pb zircon ages of the Ediacaran–Cambrian boundary strata in South China: Terra Nova, v. 27, no. 1, p. 62–68, doi:10.1111/ter.12134.
Chen, J., H. Cao, and P. Sun, 2017, Fracability evaluation of shale in the Niutitang Formation in northwestern Hunan: Geoscience Frontiers, v. 6, no. 24, p. 390–398, doi:10.13745/j.esf.yx.2017-2-50 (in Chinese with English abstract).
Cole, J. M., S. L. Goldstein, P. B. deMenocal, S. R. Hemming, and F. E. Grousset, 2009, Contrasting compositions of Saharan dust in the eastern Atlantic Ocean during the last deglaciation and African Humid Period: Earth and Planetary Science Letters, v. 278, no. 3, p. 257–266, doi:10.1016/j.epsl.2008.12.011.
Compston, W., Z. Zhang, J. A. Cooper, G. Ma, and R. J. F. Jenkins, 2008, Further SHRIMP geochronology on the early Cambrian of South China: American Journal of Science, v. 308, no. 4, p. 399–420, doi:10.2475/04.2008.01.
Duggen, S., N. Olgun, P. Croot, L. J. Hoffmann, H. Dietze, P. Delmelle, and C. Teschner, 2010, The role of airborne volcanic ash for the surface ocean biogeochemical iron–cycle: a review: Biogeosciences (BG), v. 7, no. 3, p. 827–844, doi:10.5194/bg-7-827-2010.
Dymond, J., E. Suess, and M. Lyle, 1992, Barium in deep–sea sediment: A geochemical proxy for paleoproductivity: Paleoceanography, v. 7, no. 2, p. 163–181, doi:10.1029/92PA00181.

713 Emerson, S., K. Fischer, C. Reimers, and D. Heggie, 1985, Organic carbon dynamics
714 and preservation in deep–sea sediments: Deep Sea Research Part A.
715 Oceanographic Research Papers, v. 32, no. 1, p. 1–21,
716 doi:10.1016/0198-0149(85)90014-7.
717 Fedo, C. M., H. W. Nesbitt, and G. M. Young, 1995, Unraveling the effects of
718 potassium metasomatism in sedimentary rocks and paleosols, with implications
719 for paleoweathering conditions and provenance: Geology, v. 23, no. 10, p. 921–
720 924, doi:10.1130/0091-7613(1995)023<0921:UTEOPM>2.3.CO;2.
721 Feng, W., F. Wang, J. Guan, J. Zhou, F. Wei, W. Dong, and Y. Xu, 2018, Geologic
722 structure controls on initial productions of lower Silurian Longmaxi shale in south
723 China: Marine and Petroleum Geology, v. 91, p. 163–178,
724 doi:10.1016/j.marpetgeo.2018.01.001.
725 Froelich, P. N., G. P. Klinkhammer, M. L. Bender, N. A. Luedtke, G. R. Heath, D.
726 Cullen, P. Dauphin, D. Hammond, B. Hartman, and V. Maynard, 1979, Early
727 oxidation of organic matter in pelagic sediments of the eastern equatorial Atlantic:
728 suboxic diagenesis: Geochimica et Cosmochimica Acta, v. 43, no. 7, p. 1075–
729 1090, doi:10.1016/0016-7037(79)90095-4.
730 Fuchida, S., Y. Mizuno, H. Masuda, T. Toki, and H. Makita, 2014, Concentrations and
731 distributions of amino acids in black and white smoker fluids at temperatures over
732 200°C: Organic Geochemistry, v. 66, p. 98–106,
733 doi:10.1016/j.orggeochem.2013.11.008.
734 Galloway, J. M., A. R. Sweet, G. T. Swindles, K. Dewing, T. Hadlari, A. F. Embry,
735 and H. Sanei, 2013, Middle Jurassic to Lower Cretaceous paleoclimate of
736 Sverdrup Basin, Canadian Arctic Archipelago inferred from the
737 palynostratigraphy: Marine and Petroleum Geology, v. 44, p. 240–255,
738 doi:10.1016/j.marpetgeo.2013.01.001.
739 Gao, P., Z. He, S. Li, G. G. Lash, B. Li, B. Huang, and D. Yan, 2018, Volcanic and
740 hydrothermal activities recorded in phosphate nodules from the Lower Cambrian
741 Niutitang Formation black shales in South China: Palaeogeography,
742 Palaeoclimatology, Palaeoecology, v. 505, p. 381–397,
743 doi:10.1016/j.palaeo.2018.06.019.
744 German, C., A. Campbell, and J. Edmond, 1991a, Hydrothermal scavenging at the
745 Mid-Atlantic Ridge: modification of trace element dissolved fluxes: Earth and
746 Planetary Science Letters, v. 107, no. 1, p. 101–114,
747 doi:10.1016/0012-821X(91)90047-L.
748 German, C., A. Fleer, M. Bacon, and J. Edmond, 1991b, Hydrothermal scavenging at
749 the Mid-Atlantic Ridge: radionuclide distributions: Earth and Planetary Science
750 Letters, v. 105, no. 1-3, p. 170–181, doi:10.1016/0012-821X(91)90128-5.
751 Goldberg, T., H. Strauss, Q. Guo, and C. Liu, 2007, Reconstructing marine redox
752 conditions for the Early Cambrian Yangtze Platform: Evidence from biogenic
753 sulphur and organic carbon isotopes: Palaeogeography, Palaeoclimatology,
754 Palaeoecology, v. 254, no. 1, p. 175–193, doi:10.1016/j.palaeo.2007.03.015.
755 Guo, Q., Y. Deng, D. Hippler, G. Franz, and J. Zhang, 2016, REE and trace element

patterns from organic-rich rocks of the Ediacaran–Cambrian transitional interval: Gondwana Research, v. 36, p. 94–106, doi:10.1016/j.gr.2016.03.012.
Gupta, L. P., and H. Kawahata, 2006, Downcore diagenetic changes in organic matter and implications for paleoproductivity estimates: Global and Planetary Change, v. 53, no. 1, p. 122–136, doi:10.1016/j.gloplacha.2006.01.008.
Han, T., H. Fan, X. Zhu, H. Wen, C. Zhao, and F. Xiao, 2017, Submarine hydrothermal contribution for the extreme element accumulation during the early Cambrian, South China: Ore Geology Reviews, v. 86, p. 297–308, doi:10.1016/j.oregeorev.2017.02.030.
Hao, F., H. Zou, and Y. Lu, 2013, Mechanisms of shale gas storage: Implications for shale gas exploration in China: AAPG Bulletin, v. 97, no. 8, p. 1325–1346, doi:10.1306/02141312091.
Harris, N. B., J. L. Miskimins, and C. A. Mnich, 2011, Mechanical anisotropy in the Woodford Shale, Permian Basin: Origin, magnitude, and scale: Leading Edge, v. 30, no. 3, p. 284–291, doi:10.1190/1.3567259.
Jin, C., C. Li, T. J. Algeo, N. J. Planavsky, H. Cui, X. Yang, Y. Zhao, X. Zhang, and S. Xie, 2016, A highly redox-heterogeneous ocean in South China during the early Cambrian (~529–514 Ma): Implications for biota–environment co–evolution: Earth and Planetary Science Letters, v. 441, p. 38–51, doi:10.1016/j.epsl.2016.02.019.
Jones, M. T., and S. R. Gislason, 2008, Rapid releases of metal salts and nutrients following the deposition of volcanic ash into aqueous environments: Geochimica et Cosmochimica Acta, v. 72, no. 15, p. 3661–3680, doi:10.1016/j.gca.2008.05.030.
Knoll, A. H., and S. B. Carroll, 1999, Early animal evolution: emerging views from comparative biology and geology: Science, v. 284, no. 5423, p. 2129–2137, doi:10.1126/science.284.5423.2129.
Lane, N., J. F. Allen, and W. Martin, 2010, How did LUCA make a living? Chemiosmosis in the origin of life: Bioessays, v. 32, no. 4, p. 271–280, doi:10.1002/bies.200900131.
Li, C., G. D. Love, T. W. Lyons, D. A. Fike, A. L. Sessions, and C. Xuelei, 2010, A stratified redox model for the Ediacaran ocean: Science, v. 328, no. 5974, p. 80–83, doi:10.1126/science.1182369.
Li, J., S. Tang, S. Zhang, Z. Xi, N. Yang, G. Yang, L. Li, and Y. Li, 2018, Paleo-environmental conditions of the Early Cambrian Niutitang Formation in the Fenggang area, the southwestern margin of the Yangtze Platform, southern China: Evidence from major elements, trace elements and other proxies: Journal of Asian Earth Sciences, v. 159, p. 81–97, doi:10.1016/j.jseaes.2018.03.013.
Li, L., J. Tan, D. A. Wood, Z. Zhao, D. Becker, Q. Lyu, B. Shu, and H. Chen, 2019, A review of the current status of induced seismicity monitoring for hydraulic fracturing in unconventional tight oil and gas reservoirs: Fuel, v. 242, p. 195–210, doi:10.1016/j.fuel.2019.01.026.
Li, Y., T. Fan, J. Zhang, J. Zhang, X. Wei, X. Hu, W. Zeng, and W. Fu, 2015,

Geochemical changes in the Early Cambrian interval of the Yangtze Platform, South China: Implications for hydrothermal influences and paleocean redox conditions: Journal of Asian Earth Sciences, v. 109, p. 100–123, doi:10.1016/j.jseaes.2015.05.003.

Liao, S., C. Tao, H. Li, G. Zhang, J. Liang, W. Yang, and Y. Wang, 2018, Surface sediment geochemistry and hydrothermal activity indicators in the Dragon Horn area on the Southwest Indian Ridge: Marine Geology, v. 398, p. 22–34, doi:10.1016/j.margeo.2017.12.005.

Lin, D., S. Bing, C. T. A. Lee, X. J. Shu, P. Yang, Y. Sun, Z. Tang, R. Hong, X. Lang, and H. Ma, 2015, Germanium/silicon of the Ediacaran-Cambrian Laobao cherts: Implications for the bedded chert formation and paleoenvironment interpretations: Geochemistry Geophysics Geosystems, v. 16, no. 3, p. 751–763, doi:10.1002/2014GC005595.

Lin, T., S. Bao, J. Zhang, Z. Zhou, K. Yuan, B. Li, and S. Yang, 2016, Shale gas accumulation conditions and gas–bearing characteristics of the Lower Cambrian Niutitang Formation in Well Changye-1 in northwestern Hunan Province: Petroleum Research, v. 1, no. 2, p. 205–212, doi:10.1016/S2096-2495(17)30043-1.

Little, C., and R. Vrijenhoek, 2003, Are hydrothermal vent animals living fossils?: Trends in Ecology & Evolution, v. 18, no. 11, p. 582–588, doi:10.1016/j.tree.2003.08.009.

Liu, Z., T. J. Algeo, X. Guo, J. Fan, X. Du, and Y. Lu, 2017, Paleo-environmental cyclicity in the Early Silurian Yangtze Sea (South China): Tectonic or glacio-eustatic control?: Palaeogeography, Palaeoclimatology, Palaeoecology, v. 466, p. 59–76, doi:10.1016/j.palaeo.2016.11.007.

Liu, Z. H., X. G. Zhuang, G. E. Teng, X. M. Xie, L. M. Yin, L. Z. Bian, Q. L. Feng, and T. J. Algeo, 2015, The lower Cambrian Niutitang Formation at Yantiao (Guizhou, SW China): organic matter enrichment, source rockpotential, and hydrothermal influences: Journal of Petroleum Geology, v. 38, no. 4, p. 411–432, doi:10.1111/jpg.12619.

Luo, Q., J. Hao, C. B. Skovsted, P. Luo, I. Khan, J. Wu, and N. Zhong, 2017, The organic petrology of graptolites and maturity assessment of the Wufeng–Longmaxi Formations from Chongqing, China: Insights from reflectance cross-plot analysis: International Journal of Coal Geology, v. 183, p. 161–173, doi:10.1016/j.coal.2017.09.006.

Lyu, Q., X. Long, P. G. Ranjith, J. Tan, and Y. Kang, 2018a, Experimental investigation on the mechanical behaviours of a low-clay shale under water-based fluids: Engineering Geology, v. 233, p. 124–138, doi:10.1016/j.enggeo.2017.12.002.

Lyu, Q., X. Long, P. G. Ranjith, J. Tan, Y. Kang, and Z. Wang, 2018b, Experimental investigation on the mechanical properties of a low-clay shale with different adsorption times in sub-/super-critical CO_2: Energy, v. 147, p. 1288–1298, doi:10.1016/j.energy.2018.01.084.

Mckerrow, W. S., C. R. Scotese, and M. D. Brasier, 1992, Early Cambrian continental reconstructions: Journal of the Geological Society, v. 149, no. 4, p. 599–606, doi:10.1144/gsjgs.149.4.0599.

McLennan, S. M., 1993, Weathering and Global Denudation: Journal of Geology, v. 101, no. 2, p. 295–303, doi:10.1086/648222.

Morford, J. L., W. R. Martin, R. François, and C. M. Carney, 2009, A model for uranium, rhenium, and molybdenum diagenesis in marine sediments based on results from coastal locations: Geochimica et Cosmochimica Acta, v. 73, no. 10, p. 2938–2960, doi:10.1016/j.gca.2009.02.029.

Murray, R. W., and M. Leinen, 1993, Chemical transport to the seafloor of the equatorial Pacific Ocean across a latitudinal transect at 135 W: tracking sedimentary major, trace, and rare earth element fluxes at the Equator and the Intertropical Convergence Zone: Geochimica et Cosmochimica Acta, v. 57, no. 17, p. 4141–4163, doi:10.1016/0016-7037(93)90312-K.

Taylor, S.R., and McLennan, S.M., 1985, The continental crust: its composition and evolution.

Nesbitt, H. W., and G. M. Young, 1982, Early Proterozoic climates and plate motions inferred from major element chemistry of lutites: Nature, v. 299, no. 5885, p. 715–717, doi:10.1038/299715a0.

Och, L. M., G. A. Shields-Zhou, S. W. Poulton, C. Manning, M. F. Thirlwall, D. Li, X. Chen, H. Ling, T. Osborn, and L. Cremonese, 2013, Redox changes in Early Cambrian black shales at Xiaotan section, Yunnan Province, South China: Precambrian Research, v. 225, p. 166–189, doi:10.1016/j.precamres.2011.10.005.

Ocubalidet, S. G., S. M. Rimmer, and J. A. Conder, 2018, Redox conditions associated with organic carbon accumulation in the Late Devonian New Albany Shale, west-central Kentucky, Illinois Basin: International Journal of Coal Geology, v. 190, p. 42–55, doi:10.1016/j.coal.2017.11.017.

Pi, D., C. Liu, G. Zhou, and S. Jiang, 2013, Trace and rare earth element geochemistry of black shale and kerogen in the early Cambrian Niutitang Formation in Guizhou province, South China: Constraints for redox environments and origin of metal enrichments: Precambrian Research, v. 225, no. 2013, p. 218–229, doi:10.1016/j.precamres.2011.07.004.

Piper, D. Z., and R. B. Perkins, 2004, A modern vs. Permian black shale—the hydrography, primary productivity, and water-column chemistry of deposition: Chemical Geology, v. 206, no. 3, p. 177–197, doi:10.1016/j.chemgeo.2003.12.006.

Reysenbach, A. L., and S. L. Cady, 2001, Microbiology of ancient and modern hydrothermal systems: Trends in Microbiology, v. 9, no. 2, p. 79–86, doi:10.1016/S0966-842X(00)01921-1.

Rowe, H. D., R. G. Loucks, S. C. Ruppel, and S. M. Rimmer, 2008, Mississippian Barnett Formation, Fort Worth Basin, Texas: Bulk geochemical inferences and Mo–TOC constraints on the severity of hydrographic restriction: Chemical Geology, v. 257, no. 1, p. 16–25, doi:10.1016/j.chemgeo.2008.08.006.

Schoepfer, S. D., J. Shen, H. Wei, R. V. Tyson, E. Ingall, and T. J. Algeo, 2015, Total organic carbon, organic phosphorus, and biogenic barium fluxes as proxies for paleomarine productivity: Earth-Science Reviews, v. 149, p. 23–52, doi:10.1016/j.earscirev.2014.08.017.

Scott, C., and T. W. Lyons, 2012, Contrasting molybdenum cycling and isotopic properties in euxinic versus non-euxinic sediments and sedimentary rocks: Refining the paleoproxies: Chemical Geology, v. 324–325, p. 19–27, doi:10.1016/j.chemgeo.2012.05.012.

Simoneit, B. R. T., 2004, Prebiotic organic synthesis under hydrothermal conditions: an overview: Advances in Space Research, v. 33, no. 1, p. 88–94, doi:10.1016/j.asr.2003.05.006.

Steiner, M., E. Wallis, B. D. Erdtmann, Y. Zhao, and R. Yang, 2001, Submarine-hydrothermal exhalative ore layers in black shales from South China and associated fossils–insights into a Lower Cambrian facies and bio-evolution: Palaeogeography, Palaeoclimatology, Palaeoecology, v. 169, no. 3, p. 165–191, doi:10.1016/S0031-0182(01)00208-5.

Steiner, M., G. Li, Y. Qian, M. Zhu, and B. D. Erdtmann, 2007, Neoproterozoic to Early Cambrian small shelly fossil assemblages and a revised biostratigraphic correlation of the Yangtze Platform (China): Palaeogeography, Palaeoclimatology, Palaeoecology, v. 254, no. 1, p. 67–99, doi:10.1016/j.palaeo.2007.03.046.

Sun, M., B. Yu, Q. Hu, R. Yang, Y. Zhang, B. Li, Y. B. Melnichenko, and G. Cheng, 2018, Pore structure characterization of organic-rich Niutitang shale from China: Small angle neutron scattering (SANS) study: International Journal of Coal Geology, v. 186, p. 115–125, doi:10.1016/j.coal.2017.12.006.

Tan, J., B. Horsfield, N. Mahlstedt, J. Zhang, R. di Primio, T. A. T. Vu, C. J. Boreham, G. van Graas, and B. A. Tocher, 2013, Physical properties of petroleum formed during maturation of Lower Cambrian shale in the upper Yangtze Platform, South China, as inferred from PhaseKinetics modelling: Marine and Petroleum Geology, v. 48, p. 47–56, doi:10.1016/j.marpetgeo.2013.07.013.

Tan, J., B. Horsfield, R. Fink, B. Krooss, H.-M. Schulz, E. Rybacki, J. Zhang, C. J. Boreham, G. van Graas, and B. A. Tocher, 2014a, Shale gas potential of the major marine shale formations in the Upper Yangtze Platform, South China, Part III: Mineralogical, lithofacial, petrophysical, and rock mechanical properties: Energy & Fuels, v. 28, no. 4, p. 2322–2342, doi:10.1021/ef4022703.

Tan, J., P. Weniger, B. Krooss, A. Merkel, B. Horsfield, J. Zhang, C. J. Boreham, G. v. Graas, and B. A. Tocher, 2014b, Shale gas potential of the major marine shale formations in the Upper Yangtze Platform, South China, Part II: Methane sorption capacity: Fuel, v. 129, p. 204–218, doi:10.1016/j.fuel.2014.03.064.

Taylor, S. R., 1964, Abundance of chemical elements in the continental crust: a new table: Geochimica et Cosmochimica Acta, v. 28, no. 8, p. 1273–1285, doi:10.1016/0016-7037(64)90129-2.

Taylor, S. R., and S. M. McLennan, 1985, The continental crust: Its composition and evolution, an examination of the geochemical record preserved in sedimentary

928 rocks: Journal of Geology, v. 94, no. 4, p. 632–633,
929 doi:10.1016/0031-9201(86)90093-2.
930 Tian, H., L. Pan, T. Zhang, X. Xiao, Z. Meng, and B. Huang, 2015, Pore
931 characterization of organic-rich Lower Cambrian shales in Qiannan Depression of
932 Guizhou Province, Southwestern China: Marine and Petroleum Geology, v. 62, p.
933 28–43, doi:10.1016/j.marpetgeo.2015.01.004.
934 Tribovillard, N., T. J. Algeo, T. Lyons, and A. Riboulleau, 2006, Trace metals as
935 paleoredox and paleoproductivity proxies: An update: Chemical Geology, v. 232,
936 no. 1, p. 12–32, doi:10.1016/j.chemgeo.2006.02.012.
937 Tribovillard, N., T. J. Algeo, F. Baudin, and A. Riboulleau, 2012, Analysis of marine
938 environmental conditions based onmolybdenum–uranium covariation–
939 Applications to Mesozoic paleoceanography: Chemical Geology, v. 324/325, p.
940 46–58, doi:10.1016/j.chemgeo.2011.09.009.
941 Uematsu, M., M. Toratani, M. Kajino, Y. Narita, Y. Senga, and T. Kimoto, 2004,
942 Enhancement of primary productivity in the western North Pacific caused by the
943 eruption of the Miyake-jima Volcano: Geophysical research letters, v. 31, no. 6,
944 doi:10.1029/2003GL018790.
945 Vosoughi Moradi, A., A. Sarı, and P. Akkaya, 2016, Geochemistry of the Miocene oil
946 shale (Hançili Formation) in the Çankırı-Çorum Basin, Central Turkey:
947 Implications for paleoclimate conditions, source–area weathering, provenance and
948 tectonic setting: Sedimentary Geology, v. 341, p. 289–303,
949 doi:10.1016/j.sedgeo.2016.05.002.
950 Wan, Y., S. Zhang, S. Tang, Z. Pan, and W. Wu, 2018, A comparative study of
951 characterization of lower Palaeozoic Niutitang shale in northwestern Hunan,
952 China: Journal of Natural Gas Science and Engineering, v. 53, p. 284–300,
953 doi:10.1016/j.jngse.2018.03.015.
954 Wang, D., H. Ling, S. Ulrich, X. Zhu, M. Zhu, and T. He, 2018, Coupling of ocean
955 redox and animal evolution during the Ediacaran-Cambrian transition: Nature
956 Communications, v. 9, no. 1, doi:10.1038/s41467-018-04980-5.
957 Wang, J., D. Chen, D. Yan, H. Wei, and L. Xiang, 2012, Evolution from an anoxic to
958 oxic deep ocean during the Ediacaran–Cambrian transition and implications for
959 bioradiation: Chemical Geology, v. 306–307, p. 129–138,
960 doi:10.1016/j.chemgeo.2012.03.005.
961 Wang, L., C. Liu, and H. Zhang, 2013, Tectonic and sedimentary settings of
962 evaporites in the Dengying Formation, South China Block: Implications for the
963 potential of potash formation: Acta Geoscientica Sinica, v. 34, no. 5, p. 585–593
964 doi:10.3975/cagsb.2013.05.09 (in Chinese with English abstract).
965 Wang, S., C. Zou, D. Dong, Y. Wang, X. Li, J. H. Huang, and Q. Guan, 2015, Multiple
966 controls on the paleoenvironment of the Early Cambrian marine black shales in
967 the Sichuan Basin, SW China: Geochemical and organic carbon isotopic evidence:
968 Marine and Petroleum Geology, v. 66, p. 660–672,
969 doi:10.1016/j.marpetgeo.2015.07.009.
970 Wang, X., N. J. Planavsky, C. T. Reinhard, H. Zou, J. J. Ague, Y. Wu, B. C. Gill, E. M.

971 Schwarzenbach, and B. Peucker-Ehrenbrink, 2016, Chromium isotope
972 fractionation during subduction-related metamorphism, black shale weathering,
973 and hydrothermal alteration: Chemical Geology, v. 423, p. 19–33,
974 doi:10.1016/j.chemgeo.2016.01.003.
975 Wang, Z., J. Tan, R. Boyle, J. Hilton, Z. Ma, W. Wang, Q. Lyu, X. Kang, and W. Luo,
976 2020, Episodic hydrothermal activity in South China during the early Cambrian:
977 Implications for biotic evolution: Marine and Petroleum Geology, v. 117, p.
978 104355, doi: 10.1016/j.marpetgeo.2020.104355.
979 Wedepohl, K. H., 1971, Environmental influences on the chemical composition of
980 shales and clays: Physics & Chemistry of the Earth, v. 8, no. 71, p. 307–333,
981 doi:10.1016/0079-1946(71)90020-6.
982 Wu, C., J. Tuo, M. Zhang, L. Sun, Y. Qian, and Y. Liu, 2016, Sedimentary and
983 residual gas geochemical characteristics of the Lower Cambrian organic-rich
984 shales in Southeastern Chongqing, China: Marine and Petroleum Geology, v. 75, p.
985 140–150, doi:10.1016/j.marpetgeo.2016.04.013.
986 Wu, C., J. Tuo, L. Zhang, M. Zhang, J. Li, Y. Liu, and Y. Qian, 2017, Pore
987 characteristics differences between clay-rich and clay-poor shales of the Lower
988 Cambrian Niutitang Formation in the Northern Guizhou area, and insights into
989 shale gas storage mechanisms: International Journal of Coal Geology, v. 178, p.
990 13–25, doi:10.1016/j.coal.2017.04.009.
991 Xiang, L., S. D. Schoepfer, S. Shen, C. Cao, and H. Zhang, 2017, Evolution of
992 oceanic molybdenum and uranium reservoir size around the Ediacaran–Cambrian
993 transition: Evidence from western Zhejiang, South China: Earth and Planetary
994 Science Letters, v. 464, p. 84–94, doi:10.1016/j.epsl.2017.02.012.
995 Xiao, Z., J. Tan, Y. Ju, J. Hilton, R. Yang, P. Zhou, Y. Huang, B. Ning, and J. Liu,
996 2018, Natural gas potential of Carboniferous and Permian transitional shales in
997 central Hunan, South China: Journal of Natural Gas Science and Engineering, v.
998 55, p. 520–533, doi:10.1016/j.jngse.2018.05.024.
999 Xu, L., B. Lehmann, J. Mao, W. Qu, and A. Du, 2011, Re-Os age of polymetallic
1000 Ni-Mo-PGE-Au mineralization in Early Cambrian black shales of South China—a
1001 reassessment: Economic Geology, v. 106, no. 3, p. 511–522,
1002 doi:10.2113/econgeo.106.3.511.
1003 Xu, L., B. Lehmann, J. Mao, T. F. Nägler, N. Neubert, M. E. Böttcher, and P. Escher,
1004 2012, Mo isotope and trace element patterns of Lower Cambrian black shales in
1005 South China: Multi-proxy constraints on the paleoenvironment: Chemical
1006 Geology, v. 318–319, p. 45–59, doi:10.1016/j.chemgeo.2012.05.016.
1007 Yamamoto, K., 1987, Geochemical characteristics and depositional environments of
1008 cherts and associated rocks in the Franciscan and Shimanto Terranes: Sedimentary
1009 Geology, v. 52, no. 1, p. 65–108, doi:10.1016/0037-0738(87)90017-0.
1010 Yan, D., D. Chen, Q. Wang, and J. Wang, 2012, Predominance of stratified anoxic
1011 Yangtze Sea interrupted by short-term oxygenation during the Ordo-Silurian
1012 transition: Chemical Geology, v. 291, p. 69–78,
1013 doi:10.1016/j.chemgeo.2011.09.015.

Yan, J., Y. Men, Y. Sun, Q. Yu, W. Liu, H. Zhang, J. Liu, J. Kang, S. Zhang, H. Bai, and X. Zheng, 2016, Geochemical and geological characteristics of the Lower Cambrian shales in the middle–upper Yangtze area of South China and their implication for the shale gas exploration: Marine and Petroleum Geology, v. 70, p. 1–13, doi:10.1016/j.marpetgeo.2015.11.010.

Yang, A., M. Zhu, J. Zhang, and G. Li, 2003, Early Cambrian eodiscoid trilobites of the Yangtze Platform and their stratigraphic implications: Progress in Natural Science, v. 13, no. 11, p. 861–866, doi:10.1080/10020070312331344560

Yang, C., M. Zhu, D. J. Condon, and X. Li, 2017, Geochronological constraints on stratigraphic correlation and oceanic oxygenation in Ediacaran-Cambrian transition in South China: Journal of Asian Earth Sciences, v. 140, p. 75–81, doi:10.1016/j.jseaes.2017.03.017.

Yang, C., X. Li, M. Zhu, D. J. Condon, and J. Chen, 2018, Geochronological constraint on the Cambrian Chengjiang biota, South China: Journal of the Geological Society, v. 175, no. 4, p. 659–666, doi:10.1144/jgs2017-103

Yang, R., H. Wei, M. Bao, W. Wang, Q. Wang, X. Zhang, and L. Liu, 2008, Discovery of hydrothermal venting community at the base of Cambrian barite in Guizhou Province, Western China: Implication for the Cambrian biological explosion: Progress in Natural Science, v. 18, no. 1, p. 65–70, doi:10.1016/j.pnsc.2007.07.006.

Yang, X., D. Yan, X. Wei, Z. Liwei, B. Zhang, H. Xu, Y. Gong, and J. He, 2018, Different formation mechanism of quartz in siliceous and argillaceous shales: A case study of Longmaxi Formation in South China: Marine and Petroleum Geology, v. 94, p. 80–94, doi:10.1016/j.marpetgeo.2018.03.036.

Yeasmin, R., D. Chen, Y. Fu, J. Wang, Z. Guo, and C. Guo, 2017, Climatic-oceanic forcing on the organic accumulation across the shelf during the Early Cambrian (Age 2 through 3) in the mid-upper Yangtze Block, NE Guizhou, South China: Journal of Asian Earth Sciences, v. 134, p. 365–386, doi:10.1016/j.jseaes.2016.08.019.

Yu, B., J. Li, Q. Zeng, M. Sun, and M. Shi, 2017, Depositional Environment and Diagenesis of Organic Shale: East China University of Science and Technology Press: Shanghai, 234 p.

Zhai, L., C. Wu, Y. Ye, S. Zhang, and Y. Wang, 2018, Fluctuations in chemical weathering on the Yangtze Block during the Ediacaran–Cambrian transition: Implications for paleoclimatic conditions and the marine carbon cycle: Palaeogeography, Palaeoclimatology, Palaeoecology, v. 490, p. 280–292, doi:10.1016/j.palaeo.2017.11.006.

Zhang, J., Z. Huo, X. Tan, Y. Liu, and S. Han, 2017, Shale Gas Geology in China: East China University of Science and Technology Press: Shanghai, 263 p.

Zhao, J., Z. Jin, Z. Jin, Y. Geng, X. Wen, and C. Yan, 2016, Applying sedimentary geochemical proxies for paleoenvironment interpretation of organic-rich shale deposition in the Sichuan Basin, China: International Journal of Coal Geology, v. 163, no. 2016, p. 52–71, doi:10.1016/j.coal.2016.06.015.

Zhao, J., Z. Jin, Z. Jin, X. Wen, Y. Geng, C. Yan, and H. Nie, 2017, Depositional environment of shale in Wufeng and Longmaxi Formations, Sichuan Basin: Petroleum Research, v. 2, no. 3, p. 209–221, doi:10.1016/j.ptlrs.2017.04.003.

Zheng, Y., R. F. Anderson, A. V. Geen, and J. Kuwabara, 2000, Authigenic molybdenum formation in marine sediments: a link to pore water sulfide in the Santa Barbara Basin: Geochimica et Cosmochimica Acta, v. 64, no. 24, p. 4165–4178, doi:10.1016/S0016-7037(00)00495-6.

AUTHOR VITA

JINGQIANG TAN ~ Key Laboratory of Metallogenic Prediction of Nonferrous Metals and Geological Environment Monitoring, Ministry of Education, School of Geosciences and Info-physics, Central South University, Changsha, 410083, China; tanjingqiang@csu.edu.cn

Jingqiang Tan is Professor of Petroleum Geology and Head of Department of Geological Resources at the Central South University, China. He received his Ph.D. degree from the Technical University of Berlin in Germany in 2014. His primary research interests are geological and geochemical analysis of shale gas and oil systems, and characterization and stimulation of unconventional reservoirs.

ZHANGHU WANG ~ Key Laboratory of Metallogenic Prediction of Nonferrous Metals and Geological Environment Monitoring, Ministry of Education, School of Geosciences and Info-physics, Central South University, Changsha, 410083, China; zhanghu.wang@csu.edu.cn

Zhanghu Wang is currently a Ph.D. student at Central South University. He gained his M.S. from Central South University in 2017. His research interests include sequence

1082 stratigraphy, depositional systems, and reservoir characterization. His present research
1083 includes the influence of hydrothermal activity on paleoenvironments, and
1084 unconventional shale reservoirs.
1085
1086 WENHUI WANG ~ Key Laboratory of Metallogenic Prediction of Nonferrous Metals
1087 and Geological Environment Monitoring, Ministry of Education, School of
1088 Geosciences and Info-physics, Central South University, Changsha, 410083, China;
1089 whwang@csu.edu.cn
1090 Wenghui Wang is Associate Professor of Paleontology and Stratigraphy at Central
1091 South University, China. She received her Ph.D. degree from Nanjing University in
1092 2013 where she subsequently worked as an assistant researcher until the end of 2016.
1093 Her research focusses on Palaeozoic planktonic palaeontology, palynology and
1094 stratigraphy. She is currently investigating graptolitic biostratigraphy from south
1095 China near the Cambrian/Ordovician and Ordovician/Silurian boundaries.
1096
1097 JASON HILTON ~ School of Geography, Earth and Environmental Science,
1098 University of Birmingham, Birmingham, B152TT, UK; J.M.Hilton@bham.ac.uk
1099 Jason Hilton is a Reader in Palaeobiology and Palaeoenvironments at the University
1100 of Birmingham. He received his BSc from Sheffield University in 1992, and his Ph.D.
1101 from Cardiff University in 1996. His wide-ranging, multidisciplinary research
1102 focusses on palaeobotany, sedimentology, stratigraphy and palaeonvironments. Since
1103 2003, he has worked extensively on resource-bearing sedimentary successions in

China.

JIANHUA GUO ~ Key Laboratory of Metallogenic Prediction of Nonferrous Metals and Geological Environment Monitoring, Ministry of Education, School of Geosciences and Info-physics, Central South University, Changsha, 410083, China; gjh796@csu.edu.cn

Jianhua Guo is a Professor of Petroleum Geology at Central South University, China. He has more than 30 years experience working in the petroleum industry. His primary research interests are sedimentology and basin analysis.

XIKAI WANG ~ Key Laboratory of Metallogenic Prediction of Nonferrous Metals and Geological Environment Monitoring, Ministry of Education, School of Geosciences and Info-physics, Central South University, Changsha, 410083, China; 852303596@qq.com

Xikai Wang obtained his Masters' degree in Petroleum Geology at the Central South University in China in 2019. He is currently a Ph.D. candidate at the University of North Carolina at Chapel Hill in the United States. His research focuses on shale gas geology and basin analysis.

Figures

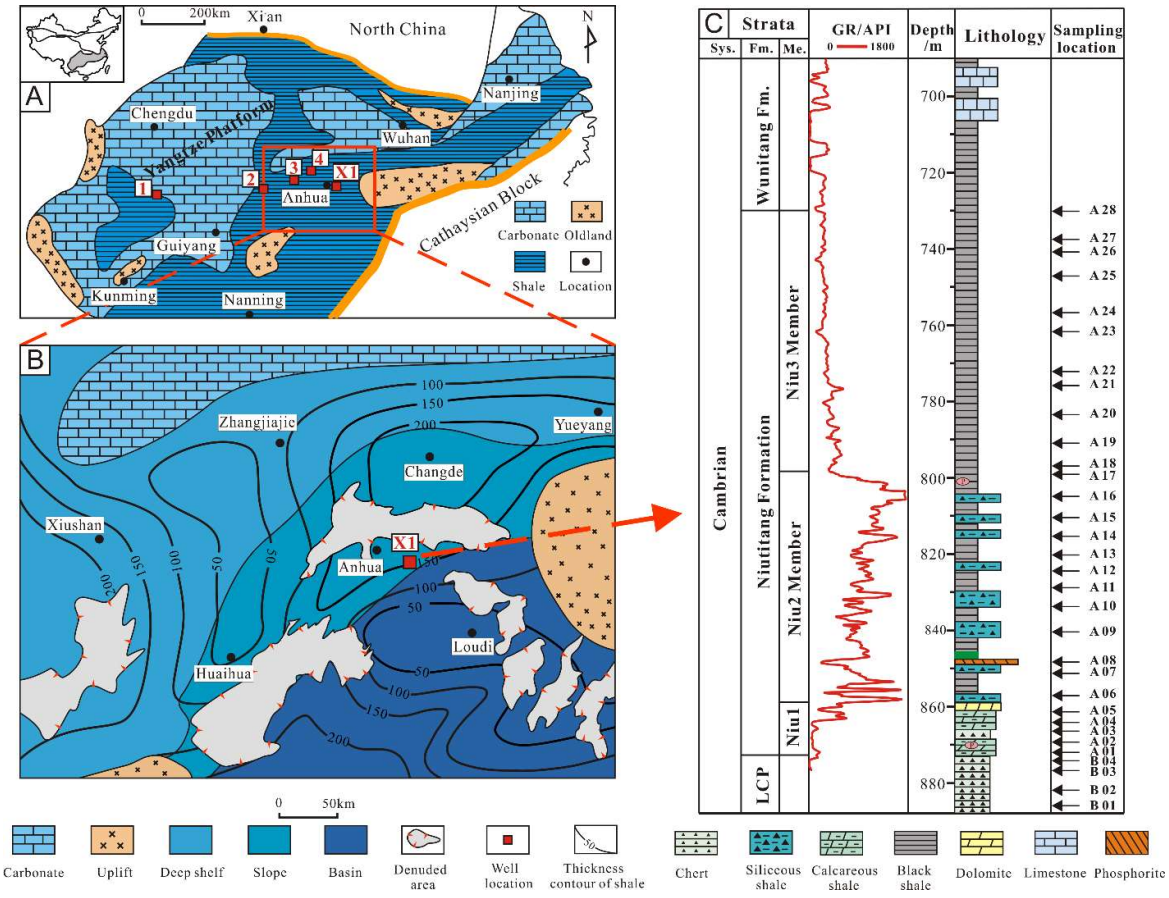

Figure 1. (A) Paleogeographic map of the Yangtze Platform in the early Cambrian, modified after Wang et al. (2012). Selected sections include: 1 - Xiaotan, 2 - Songtao, 3 - Longbizui, 4 – Ganziping; (B) Early Cambrian paleogeographic map showing lithofacies distribution in the Xuefeng Uplift area and sampling sites; (C) Stratigraphic column of the Niutitang Formation of the X1 well and sampling depths.

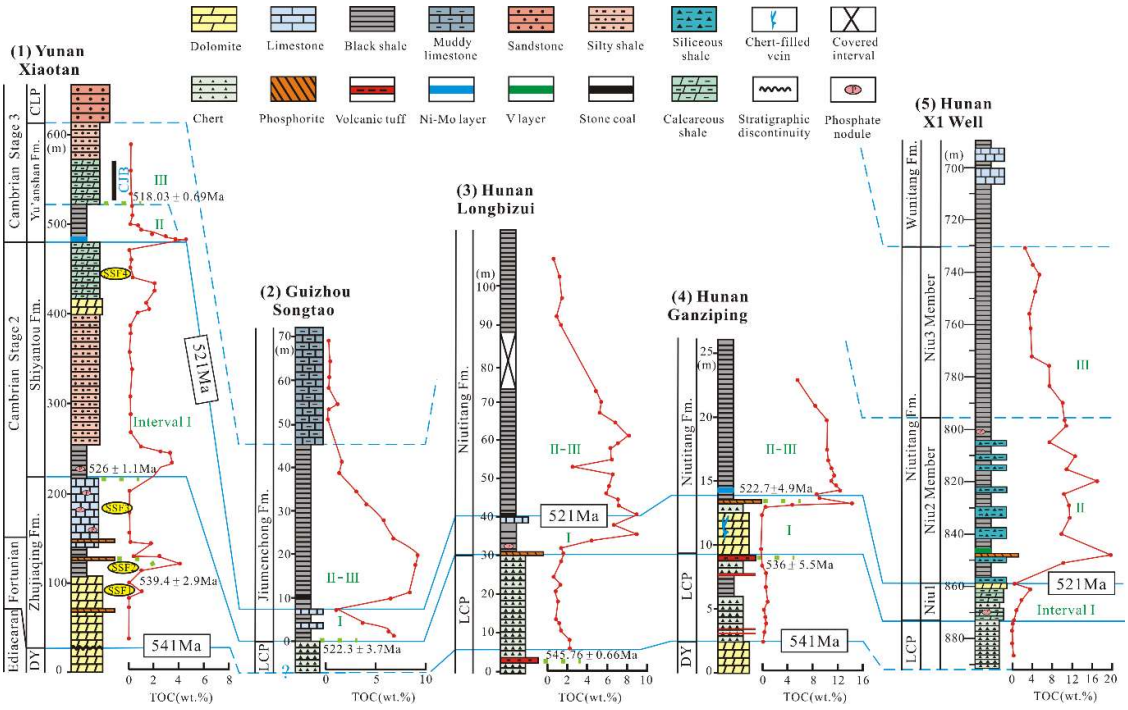

Figure 2. Stratigraphic correlation with biostratigraphic and tuff/ore dating of the early Cambrian (ca. 541-514 Ma) sections across South China. Intervals I, II, and III are mainly modified after Jin et al. (2016). Data source: 1 – Xiaotan (Yang et al., 2003; Och et al., 2013); 2 – Songtao (Yang et al., 2003; Goldberg et al., 2007); 3 – Longbizui (Wang et al., 2012; Yang et al., 2017); 4 –Ganziping (Chen et al., 2009); 5 – X1 (this study). U–Pb ages of the Xiaotan and Songtao sections are from adjacent Meishucun (Compston et al., 2008), Maotianshan (Yang et al., 2018a), and Bahuang (Chen et al., 2015), respectively. Abbreviations: CLP = Canglangpu Formation, DY = Dengying Formation, LCP = Liuchapo Formation, CJB = Chengjiang Biota.

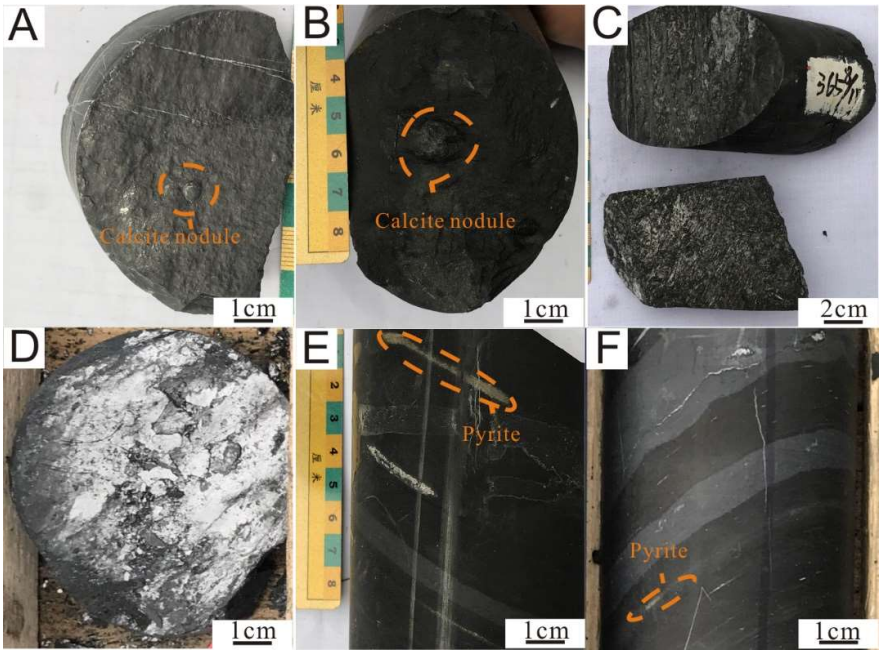

Figure 3. Lithologies of samples from X1 well. (A) Calcite patches in dark gray calcareous shale, 869.4m (2852.4 ft); (B) Calcite patches in dark gray calcareous shale, 864.3m (2835.6 ft); (C) Black siliceous shale, 850.1m (2789.1 ft); (D) Black shale with intense graphite reflectance, 848.2m (2782.8 ft); (E) Pyrite bands in black siliceous shale, 840.8m (2758.5 ft); (F) Black siliceous shale interbedded with gray-black mudstone, 813.4m (2668.6 ft).

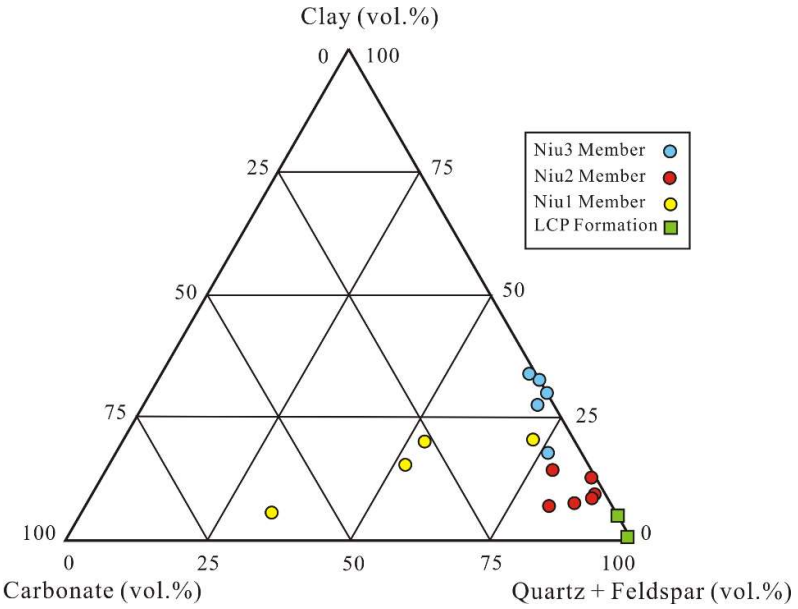

1149

1150 **Figure 4.** Ternary diagram of minerals from the Niutitang shale Niu1, Niu2 and Niu3

1151 members and the underlying Liuchapo chert (LCP).

1152

1153

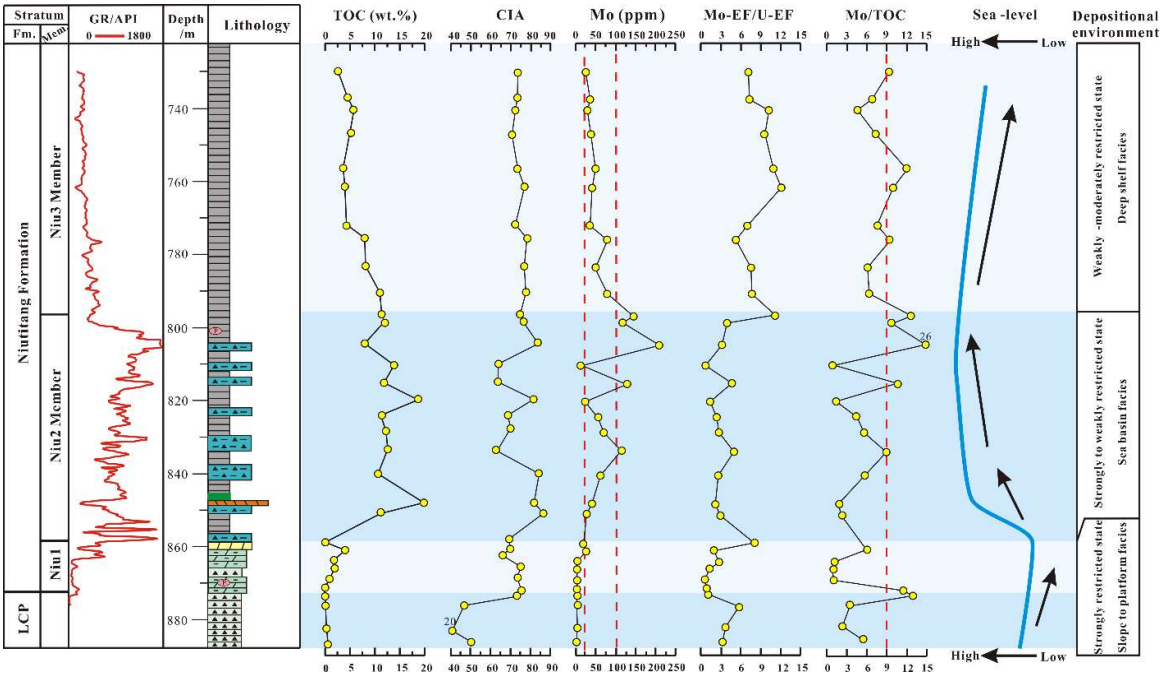

1154

1155 **Figure 5.** Stratigraphic distribution of TOC contents (wt.%), CIA, redox proxies (Mo,

1156 Mo_{EF}/U_{EF}), seawater restriction, and inferred sea-level changes. LCP = Liuchapo

1157 Formation.

1158

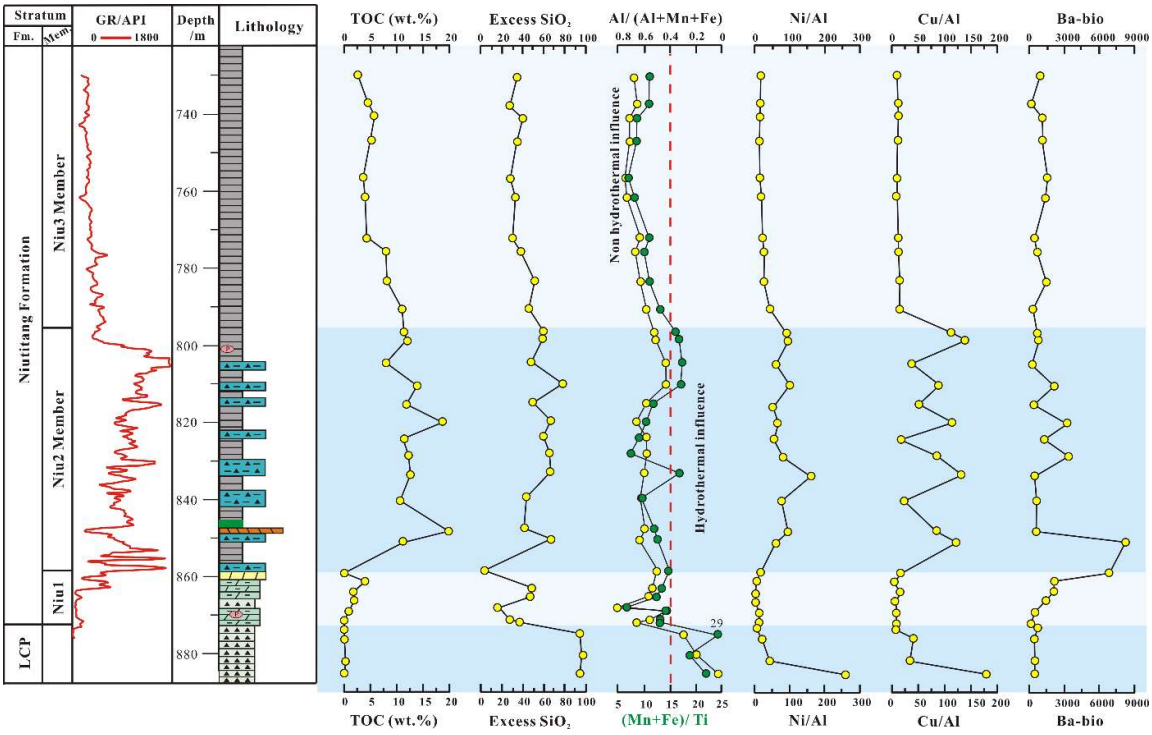

1159

1160 **Figure 6.** Stratigraphic distribution of TOC contents (wt.%), excess SiO_2 contents

1161 (wt.%), hydrothermal proxies, and paleoproductivity proxies (Ba_{bio}, Cu/Al, Ni/Al).

1162

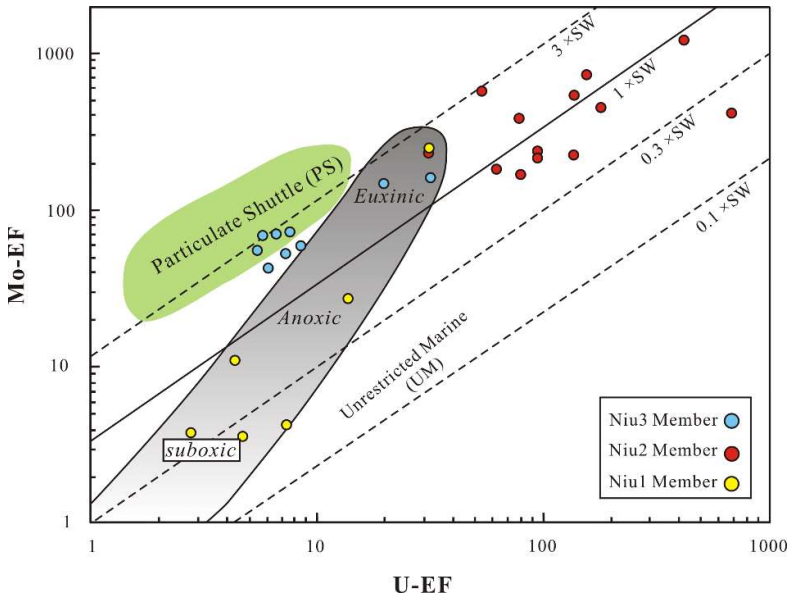

Figure 7. Mo_{EF} vs. U_{EF} Plot. The solid line represents Mo/U ratios of sea water. The dash lines represent multiples ($0.3^{\times}$, $1^{\times}$, and $3^{\times}$) of Mo/U ratios of modern seawater. The gray area represents the unrestricted marine trend and the green area represents the particulate shuttle trend. Modified after Algeo and Tribovillard (2009) and Tribovillard et al. (2012).

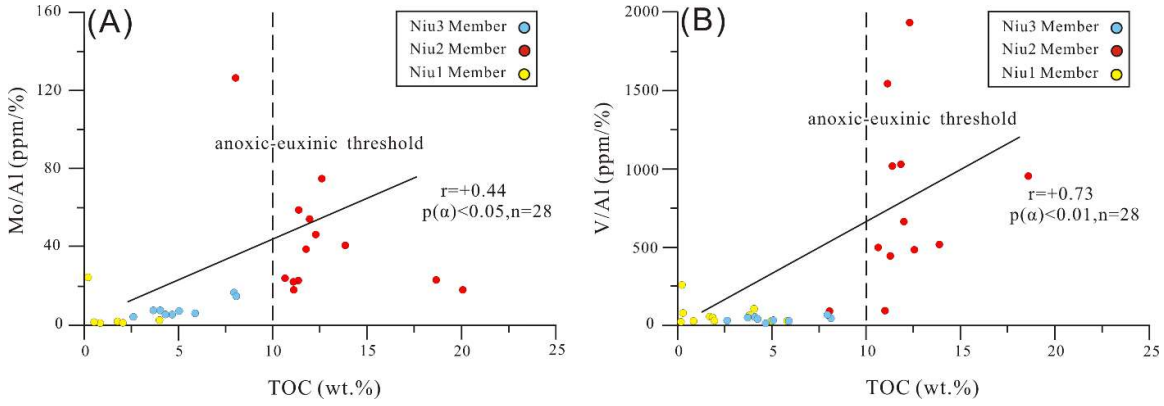

Figure 8. TOC contents vs. Mo/Al (A) and V/Al (B).

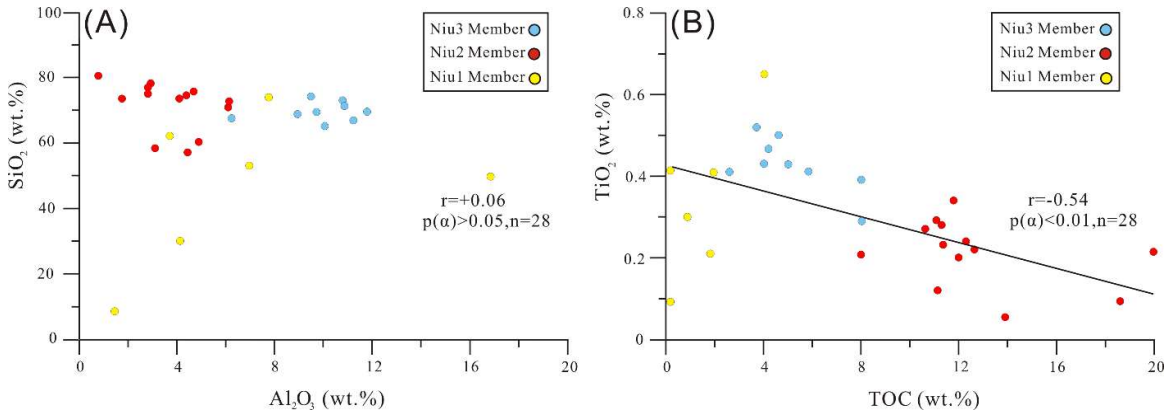

1172

1173 **Figure 9.** Al_2O_3 contents vs. SiO_2 contents (A) and TOC contents vs. TiO_2 contents

1174 (B).

1175

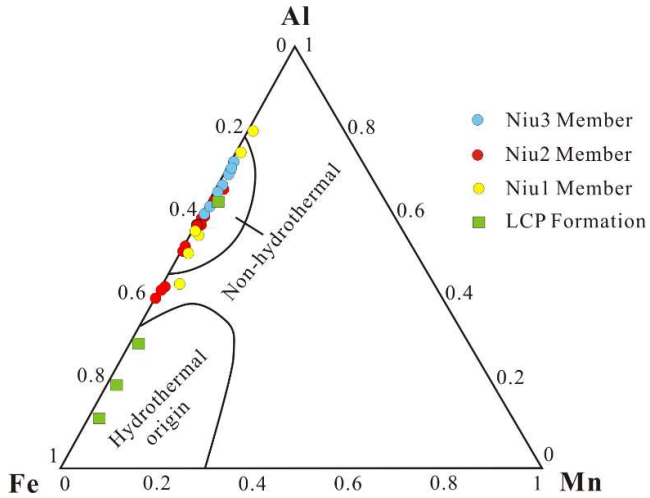

1176

1177 **Figure 10.** Al-Fe-Mn ternary diagram showing Liuchapo cherts (LCP) are from

1178 intense hydrothermal source, excess silica of the Niu1 and Niu2 shales are from

1179 hydrothermal and biogenic sources but that of the Niu3 shale is primarily biogenic

1180 origin. Position of hydrothermal and biogenic chert origins from Adachi et al. (1986)

1181 and Yamamoto (1987).

1182

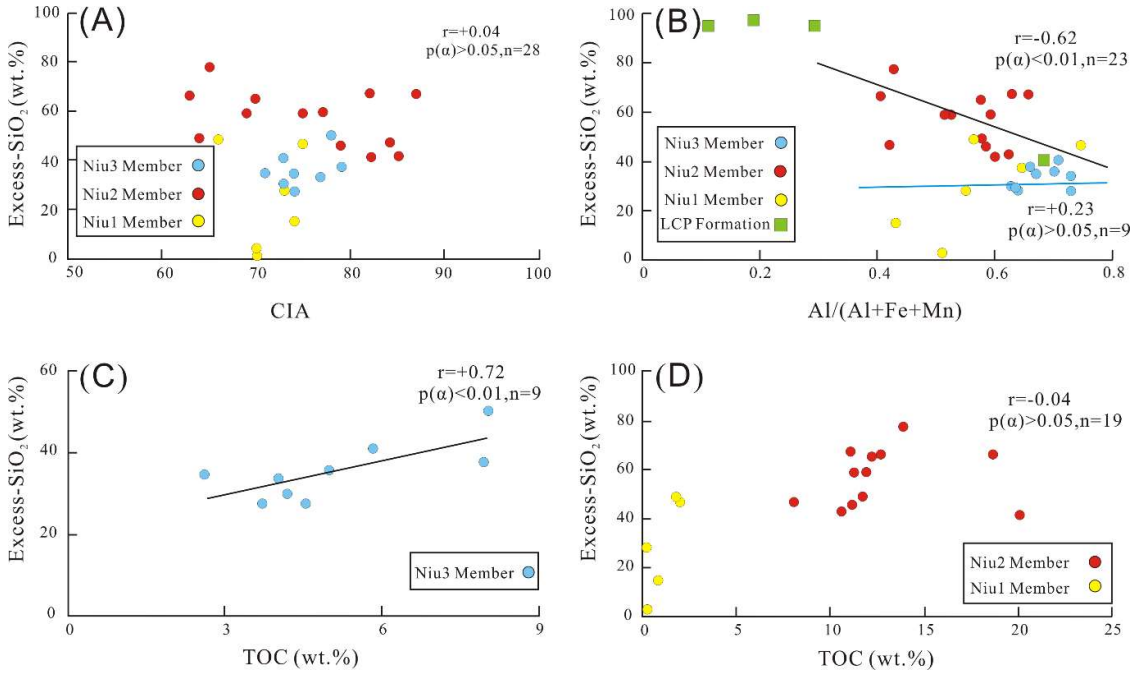

Figure 11. Excess SiO_2 contents vs paleoclimate proxies (A), excess SiO_2 contents vs. hydrothermal proxies (B), TOC contents vs. excess SiO_2 of Niu3 samples (C), and TOC contents vs. excess SiO_2 of Niu1 and Niu2 samples (D).

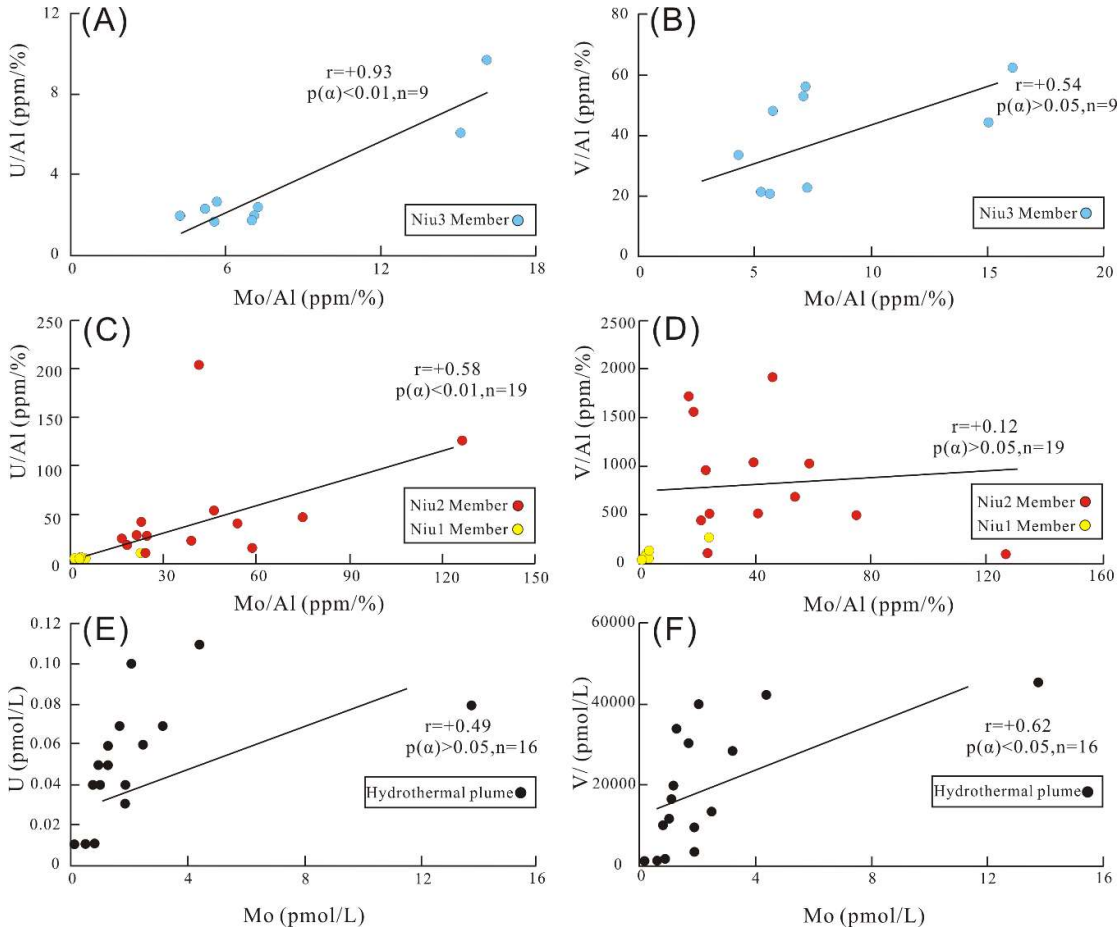

1188

1189 **Figure 12.** Correlations among redox metal elements. U/Al vs. Mo/Al ratios (A) and

1190 V/Al vs. Mo/Al ratios (B)in Niu3 samples; U/Al vs. Mo/Al ratios (C) and V/Al vs.

1191 Mo/Al ratios (D) in Niu1 and Niu2 samples; U concentration vs. Mo concentration (E)

1192 and V concentration vs. Mo concentration (F) in particles from the Mid-Atlantic

1193 Ridge hydrothermal plume.

1194

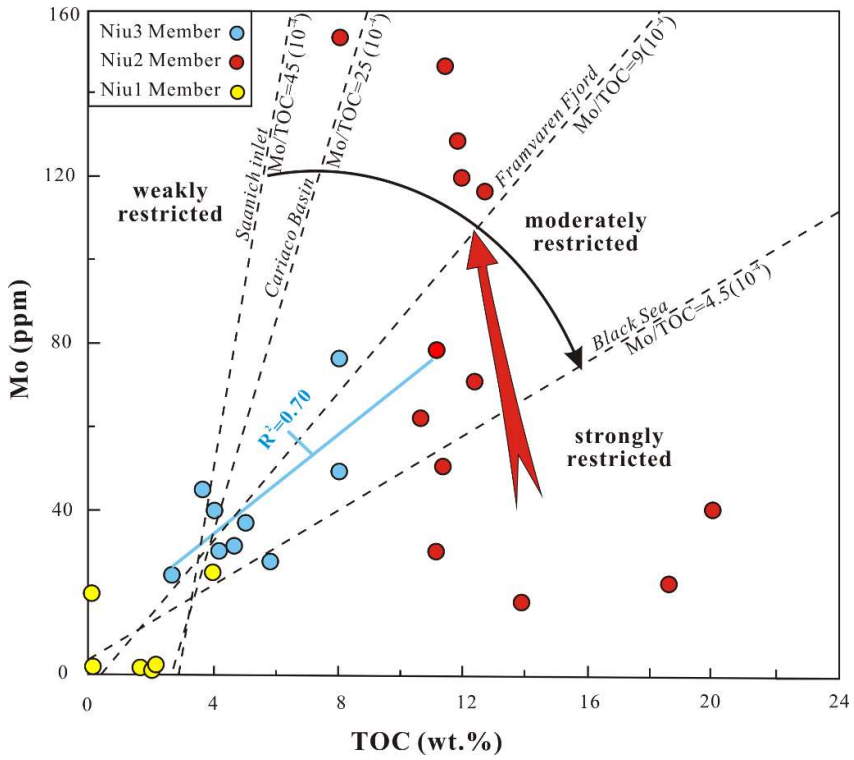

1195

1196 **Figure 13.** Mo concentrations vs. TOC contents. Dashed lines represent four modern

1197 anoxic basin systems in Saanich Inlet, Cariaco Basin, Framvaren Fjord, and Black sea

1198 (Algeo and Lyons, 2006; Algeo et al., 2007), showing different seawater restriction

1199 environments.

1200

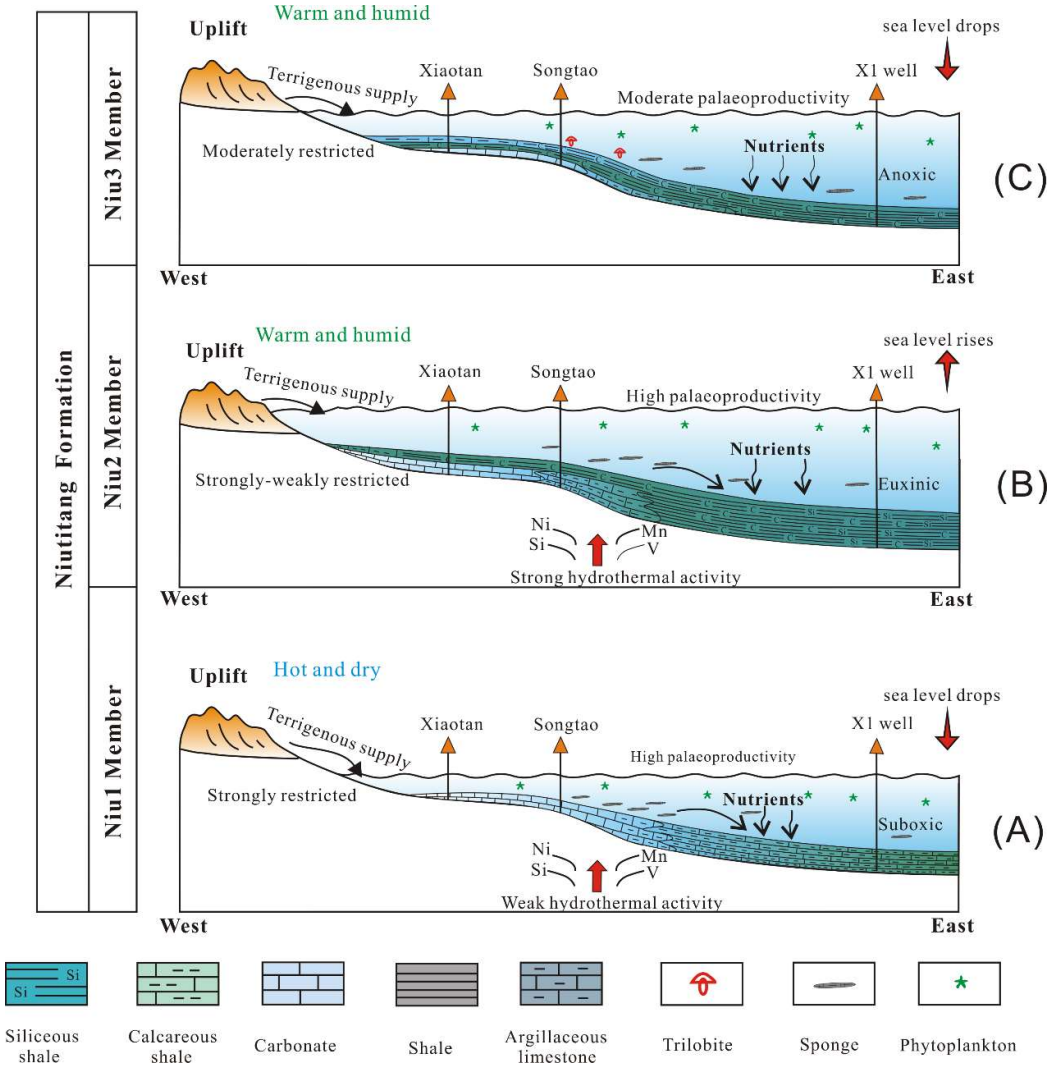

1201

1202 **Figure 14.** Depositional models and inferred paleoclimates of the Lower Cambrian

1203 sedimentary rocks in the eastern Xuefeng Uplift through the Niutitang Formation.

1204

Tables

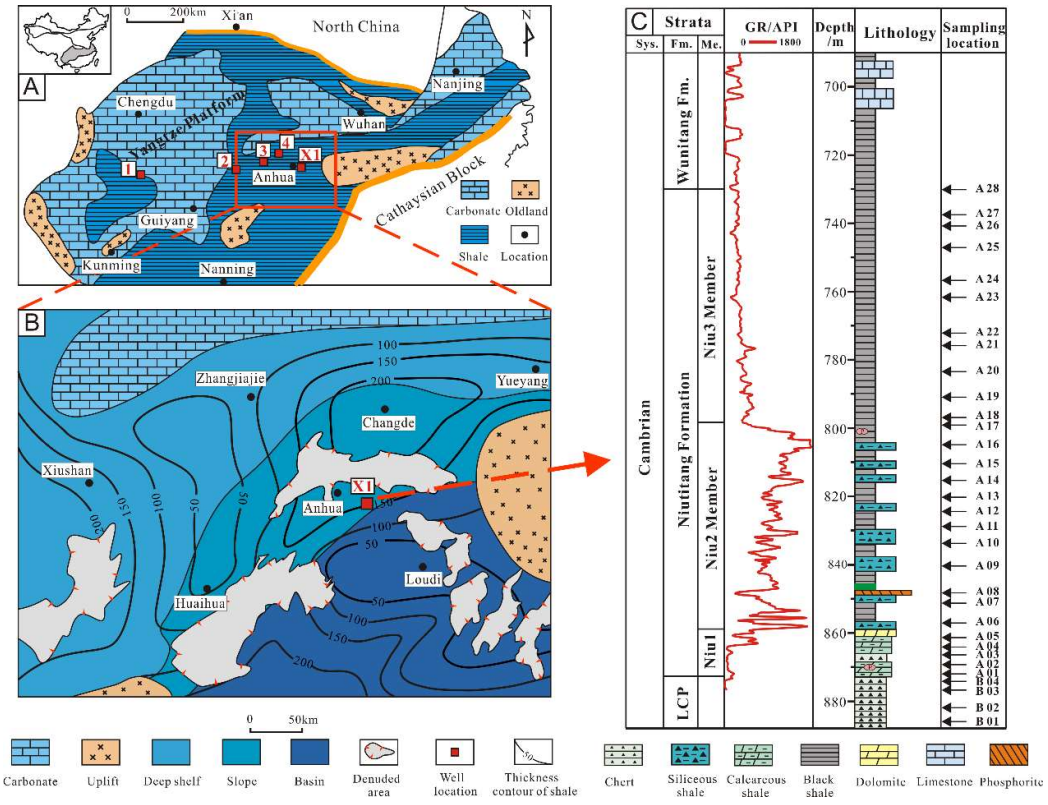

1206

1207

1208 **Table 1.** Mineral compositions of the analyzed samples.

Sample	Formation	Member	Lithology	Mineral Composition (vol.%)								
				Quartz	Feldspar	Calcite	Dolomite	Pyrite	Barite	Anhydrite	Glauberite	Clay
A28	Niutitang	Niu3	Shale	59.6	2.0	0.0	0.0	7.5	0.0	0.9	0.0	30.0
A27	Niutitang	Niu3	Shale	58.3	1.3	0.9	0.0	5.9	0.0	2.5	0.0	31.1
A25	Niutitang	Niu3	Shale	62.1	3.0	2.8	0.0	5.1	0.0	0.9	0.0	26.1
A23	Niutitang	Niu3	Shale	60.9	3.0	0.0	0.0	7.5	0.0	1.2	0.0	27.4
A20	Niutitang	Niu3	Shale	71.7	0.0	5.9	0.0	6.0	0.0	0.0	0.0	16.4
A18	Niutitang	Niu2	Siliceous shale	81.8	0.0	0.5	0.0	5.2	0.0	0.0	0.0	12.5
A16	Niutitang	Niu2	Shale	75.7	0.0	10.3	0.0	7.2	0.0	0.0	0.0	6.8
A14	Niutitang	Niu2	Shale	68.1	5.1	1.4	4.9	6.8	0.0	0.0	0.0	13.7
A12	Niutitang	Niu2	Siliceous shale	79.8	4.6	1.9	0.7	4.6	0.0	0.0	0.0	8.4
A10	Niutitang	Niu2	Siliceous shale	78.5	3.3	2.1	0.0	7.7	0.0	0.0	0.0	8.4
A08	Niutitang	Niu2	Shale	49.3	1.1	3.8	0.0	9.5	2.7	0.0	29.0	4.6
A06	Niutitang	Niu1	Dolomite	28.2	3.3	1.3	56.3	5.5	0.0	0.0	0.0	5.4
A05	Niutitang	Niu1	Calcareous shale	28.2	16.3	10.1	12.4	12.2	0.0	0.0	3.8	17.0
A03	Niutitang	Niu1	Siliceous shale	68.2	2.4	7.2	0.0	1.9	0.0	0.0	0.0	20.3
A01	Niutitang	Niu1	Calcareous shale	49.1	0.0	0.0	30.5	5.6	0.0	0.0	0.0	14.8
B03	Liuchapo		Chert	94.4	0.0	0.0	0.0	0.0	0.0	0.0	0.0	5.6
B01	Liuchapo		Chert	100.0	0.0	0.0	0.0	0.0	0.0	0.0	0.0	0.0

1209

1210

1211

1212 **Table 2.** TOC contents and major elements of the analyzed samples.

Sample	Formation	Member	Lithology	Depth/m	TOC (wt.%)	Major element (wt.%)										
						SiO_2	Al_2O_3	FeO	Fe_2O_3	TiO_2	Na_2O	MgO	K_2O	CaO	P_2O_5	MnO
A28	Niutitang	Niu3	Shale	730.0	2.61	72.92	10.81	0.51	3.40	0.41	0.11	1.43	3.22	0.35	0.05	0.01
A27	Niutitang	Niu3	Shale	737.3	4.59	67.25	11.27	0.41	4.28	0.50	0.31	1.29	2.70	0.79	0.07	0.01
A26	Niutitang	Niu3	Shale	740.6	5.83	74.22	9.49	0.26	2.66	0.41	0.20	1.10	2.70	0.41	0.06	0.01
A25	Niutitang	Niu3	Shale	746.9	4.99	69.68	9.75	0.21	2.88	0.43	0.36	1.07	2.54	2.00	0.07	0.02
A24	Niutitang	Niu3	Shale	756.5	3.70	69.50	11.80	0.36	2.88	0.52	0.15	1.40	3.38	0.89	0.08	0.01
A23	Niutitang	Niu3	Shale	761.5	4.02	71.70	10.87	0.31	2.71	0.43	0.08	1.34	2.74	0.44	0.06	0.01
A22	Niutitang	Niu3	Shale	772.0	4.20	65.62	10.15	0.31	4.13	0.47	0.18	2.10	2.83	2.73	0.12	0.04
A21	Niutitang	Niu3	Shale	775.7	7.99	69.03	8.94	0.26	3.18	0.39	0.06	1.20	2.02	0.60	0.09	0.01
A20	Niutitang	Niu3	Shale	783.4	8.05	72.24	6.22	0.26	2.54	0.29	0.06	1.13	1.48	2.50	0.08	0.02
A19	Niutitang	Niu2	Shale	790.6	11.10	67.74	6.25	0.46	2.84	0.29	0.03	1.11	1.43	1.42	0.08	0.01
A18	Niutitang	Niu2	Siliceous shale	796.8	11.40	75.60	4.66	0.26	2.90	0.23	0.06	0.85	1.25	0.46	0.06	0.01
A17	Niutitang	Niu2	Shale	798.6	11.98	73.60	4.14	0.21	2.67	0.20	0.01	0.76	1.11	2.35	0.82	0.03
A16	Niutitang	Niu2	Shale	804.7	8.05	58.23	3.12	0.31	2.85	0.21	0.09	4.17	0.28	3.00	0.34	0.02
A15	Niutitang	Niu2	Siliceous shale	810.3	13.88	80.52	0.82	0.36	0.42	0.06	0.07	0.41	0.20	1.50	0.03	0.01
A14	Niutitang	Niu2	Shale	815.3	11.78	70.88	6.18	0.36	3.03	0.34	0.51	0.90	1.66	1.28	0.21	0.01
A13	Niutitang	Niu2	Shale	820.1	18.63	73.34	1.79	0.26	0.40	0.09	0.03	1.02	0.28	1.06	0.02	0.02
A12	Niutitang	Niu2	Siliceous shale	824.3	11.30	74.63	4.40	0.46	1.75	0.28	0.15	0.78	1.35	0.74	0.09	0.01
A11	Niutitang	Niu2	Siliceous shale	828.7	12.30	75.59	2.91	0.36	1.17	0.24	0.14	1.00	0.75	1.81	0.24	0.02
A10	Niutitang	Niu2	Siliceous shale	833.6	12.63	76.81	2.89	0.26	2.93	0.22	0.39	1.29	0.95	0.56	0.16	0.01
A09	Niutitang	Niu2	Shale	840.2	10.60	60.29	4.90	0.46	1.69	0.27	0.08	1.58	0.56	0.56	0.08	0.01
A08	Niutitang	Niu2	Shale	848.2	20.10	57.07	4.46	0.21	2.02	0.22	0.14	0.85	0.67	4.62	2.87	0.01
A07	Niutitang	Niu2	Siliceous shale	851.1	11.15	78.07	2.97	0.26	1.03	0.12	0.08	0.60	0.17	0.34	0.04	0.01

A06	Niutitang	Niu1	Dolomite	859.0	0.18	8.29	1.52	0.21	0.85	0.09	0.02	17.70	0.55	25.89	0.05	0.02
A05	Niutitang	Niu1	Calcareous shale	861.2	4.03	49.72	16.86	0.31	2.75	0.65	0.18	1.86	6.01	1.38	0.06	0.01
A04	Niutitang	Niu1	Calcareous shale	864.0	1.80	62.23	3.76	0.31	1.83	0.21	0.06	5.65	1.63	7.35	0.03	0.02
A03	Niutitang	Niu1	Siliceous shale	866.2	1.96	74.21	7.76	0.41	1.48	0.41	0.07	1.52	2.21	3.17	0.04	0.03
A02	Niutitang	Niu1	Calcareous shale	869.3	0.87	30.07	4.17	0.41	3.38	0.30	0.01	10.10	1.35	17.35	2.03	0.24
A01	Niutitang	Niu1	Calcareous shale	872.0	0.11	52.99	6.97	0.36	3.68	0.42	0.01	7.60	2.12	7.95	0.1	0.12
B04	Liuchapo		Siliceous shale	873.2	0.16	70.32	9.34	0.31	3.49	0.34	0.03	3.54	2.99	2.00	0.01	0.00
B03	Liuchapo		Chert	876.1	0.28	95.92	0.41	0.21	0.51	0.03	0.10	0.21	0.13	0.15	0.01	0.01
B02	Liuchapo		Chert	881.9	0.30	98.59	0.19	0.26	0.32	0.04	0.18	0.27	0.15	0.11	0.01	0.01
B01	Liuchapo		Chert	885.3	0.35	95.43	0.11	0.31	0.29	0.02	0.01	0.26	0.07	0.22	0.13	0.01

1217 **Table 3.** Trace element composition of the analyzed samples.

Sample	Formation	Member	Lithology	Depth/m	Trace element (ppm)									
					V	Cr	Co	Ni	Cu	Sr	Mo	Th	U	Ba
A28	Niutitang	Niu3	Shale	730.0	190	57	13	70	53	25	24	9	11	1304
A27	Niutitang	Niu3	Shale	737.3	127	59	13	76	63	54	31	10	14	532
A26	Niutitang	Niu3	Shale	740.6	103	47	11	61	56	25	28	7	8	1450
A25	Niutitang	Niu3	Shale	746.9	118	45	12	53	49	76	37	9	12	1456
A24	Niutitang	Niu3	Shale	756.5	348	61	13	91	44	40	45	7	13	1902
A23	Niutitang	Niu3	Shale	761.5	308	56	12	91	46	29	41	6	10	1732
A22	Niutitang	Niu3	Shale	772.0	257	65	11	95	57	107	31	8	14	911
A21	Niutitang	Niu3	Shale	775.7	292	60	12	119	55	31	76	6	46	1058
A20	Niutitang	Niu3	Shale	783.4	145	38	9	85	44	82	50	4	20	1588
A19	Niutitang	Niu2	Shale	790.6	308	46	10	132	45	42	78	5	32	494
A18	Niutitang	Niu2	Siliceous shale	796.8	2510	80	8	221	272	23	145	3	40	720
A17	Niutitang	Niu2	Shale	798.6	1449	60	8	206	301	82	118	3	92	824
A16	Niutitang	Niu2	Shale	804.7	151	35	10	100	60	166	209	3	207	257
A15	Niutitang	Niu2	Siliceous shale	810.3	227	11	1	43	38	90	18	1	89	2160
A14	Niutitang	Niu2	Shale	815.3	3364	133	9	186	169	69	128	2	78	482
A13	Niutitang	Niu2	Shale	820.1	908	32	2	63	107	64	22	1	39	3352
A12	Niutitang	Niu2	Siliceous shale	824.3	1033	52	8	125	39	74	56	2	66	1426
A11	Niutitang	Niu2	Siliceous shale	828.7	2978	102	5	124	131	160	71	1	82	3387
A10	Niutitang	Niu2	Siliceous shale	833.6	746	41	10	247	201	56	115	1	73	401
A09	Niutitang	Niu2	Shale	840.2	1273	62	10	197	49	39	62	2	74	673
A08	Niutitang	Niu2	Shale	848.2	4075	744	4	223	193	434	40	1	56	752
A07	Niutitang	Niu2	Siliceous shale	851.1	2426	181	2	96	191	44	29	1	30	8382

A06	Niutitang	Niu1	Dolomite	859.0	210	185	3	14	12	544	20	2	8	6939
A05	Niutitang	Niu1	Calcareous shale	861.2	936	258	7	43	32	45	24	5	38	2760
A04	Niutitang	Niu1	Calcareous shale	864.0	113	67	2	8	27	117	2	2	3	2196
A03	Niutitang	Niu1	Siliceous shale	866.2	102	84	4	11	19	51	2	5	4	1735
A02	Niutitang	Niu1	Calcareous shale	869.3	49	36	7	26	17	400	1	6	5	556
A01	Niutitang	Niu1	Calcareous shale	872.0	70	51	8	35	29	162	1	5	5	315
B04	Liuchapo		Siliceous shale	873.2	230	129	4	22	37	46	2	6	7	1035
B03	Liuchapo		Chert	876.1	16	15	1	4	9	5	1	1	1	324
B02	Liuchapo		Chert	881.9	17	14	1	5	4	5	1	1	1	382
B01	Liuchapo		Chert	885.3	41	21	1	15	225	8	2	1	2	287

1221 **Table 4.** Element ratios of the analyzed samples.

Sample	Formation	Member	Lithology	Depth/m	CIA	Al/(Al+Fe+Mn)	U_{EF}	Mo_{EF}	V_{EF}	Ni/Al	Cu/Al	Ba_{bio}	Excess-SiO_2
A28	Niutitang	Niu3	Shale	730.00	74	0.67	6.03	42.46	2.21	12.16	9.19	875	34.85
A27	Niutitang	Niu3	Shale	737.30	74	0.64	7.30	52.46	1.42	12.80	10.58	85	27.56
A26	Niutitang	Niu3	Shale	740.60	73	0.71	5.44	55.73	1.37	12.04	11.05	1073	40.80
A25	Niutitang	Niu3	Shale	746.90	71	0.70	7.56	72.46	1.52	10.35	9.51	1069	35.35
A24	Niutitang	Niu3	Shale	756.50	74	0.73	6.56	71.55	3.71	14.52	7.06	1433	27.95
A23	Niutitang	Niu3	Shale	761.50	77	0.73	5.72	70.38	3.57	15.83	8.03	1300	33.42
A22	Niutitang	Niu3	Shale	772.00	73	0.63	8.34	56.95	3.19	17.75	10.51	508	29.88
A21	Niutitang	Niu3	Shale	775.70	79	0.66	31.28	161.00	4.11	25.14	11.58	703	37.55
A20	Niutitang	Niu3	Shale	783.40	78	0.62	19.59	150.63	2.94	25.72	13.48	1341	50.34
A19	Niutitang	Niu2	Shale	790.60	79	0.58	31.00	235.13	6.21	39.89	13.63	246	45.73
A18	Niutitang	Niu2	Siliceous shale	796.80	75	0.52	52.69	587.74	67.83	89.58	110.25	535	59.19
A17	Niutitang	Niu2	Shale	798.60	77	0.52	135.40	538.38	44.07	93.99	137.33	660	59.02
A16	Niutitang	Niu2	Shale	804.70	84	0.42	404.26	1265.31	6.09	60.36	36.32	133	47.24
A15	Niutitang	Niu2	Siliceous shale	810.30	65	0.43	657.62	414.63	34.86	98.82	87.07	2127	77.63
A14	Niutitang	Niu2	Shale	815.30	64	0.58	76.61	391.23	68.55	56.85	51.65	237	49.12
A13	Niutitang	Niu2	Shale	820.10	82	0.66	133.10	230.04	63.88	66.80	112.91	3281	67.04
A12	Niutitang	Niu2	Siliceous shale	824.30	69	0.59	91.40	217.22	29.56	53.66	16.61	1251	59.14
A11	Niutitang	Niu2	Siliceous shale	828.70	70	0.58	171.49	458.92	128.87	80.49	85.03	3271	65.34
A10	Niutitang	Niu2	Siliceous shale	833.60	63	0.40	153.28	751.63	32.51	161.44	131.37	286	66.63
A09	Niutitang	Niu2	Shale	840.20	85	0.63	91.65	237.46	32.72	75.94	19.00	478	43.03
A08	Niutitang	Niu2	Shale	848.20	82	0.60	76.78	168.56	115.06	61.31	81.74	575	41.36
A07	Niutitang	Niu2	Siliceous shale	851.10	87	0.63	60.52	185.07	102.86	16.90	121.47	8264	67.61
A06	Niutitang	Niu1	Dolomite	859.00	70	0.51	30.67	244.81	17.40	16.90	15.29	6879	2.94

A05	Niutitang	Niu1	Calcareous shale	861.20	70	0.80	13.66	27.34	6.99	4.85	3.54	2091	0.00
A04	Niutitang	Niu1	Calcareous shale	864.00	66	0.56	4.34	11.00	3.78	4.15	13.61	2047	48.99
A03	Niutitang	Niu1	Siliceous shale	866.20	75	0.75	2.77	3.70	1.66	2.58	4.67	1427	46.88
A02	Niutitang	Niu1	Calcareous shale	869.30	74	0.43	7.42	4.12	1.46	11.82	7.84	390	15.39
A01	Niutitang	Niu1	Calcareous shale	872.00	75	0.56	4.63	3.47	1.26	9.49	7.83	38	28.45
B04	Liuchapo		Siliceous shale	873.2	74	0.65	4.75	4.23	3.10	4.49	7.54	664	37.43
B03	Liuchapo		Chert	876.1	47	0.29	7.88	45.61	4.98	19.40	39.99	308	94.48
B02	Liuchapo		Chert	881.9	20	0.19	21.17	76.55	11.40	45.93	35.39	375	97.92
B01	Liuchapo		Chert	885.3	50	0.12	108.57	348.59	47.05	260.13	178.52	282	95.04

1222